A variable resolution surface wave dispersion study of Eurasia, North Africa, and surrounding regions

Michael E. Pasyanos
Earth Science Division, Lawrence Livermore National Laboratory, Livermore, California, USA

Received 24 March 2005; revised 25 July 2005; accepted 14 September 2005; published 7 December 2005.

[1] This paper presents the results of a large-scale study of surface wave dispersion performed across Eurasia and North Africa. Improvements were made to previous surface wave work by enlarging the study region, increasing path density, improving spatial resolution, and expanding the period range. This study expands the coverage area northward and eastward relative to a previous dispersion analysis, which covered only North Africa and the Middle East. We have significantly increased the number of seismograms examined and group velocity measurements made. We have now made good quality dispersion measurements for about 30,000 Rayleigh wave and 20,000 Love wave paths and have incorporated measurements from several other researchers into the study. We have improved the inversion from the previous study by adopting a variable smoothness with the conjugate gradient method for the group velocity tomography. This technique produces higher-resolution models where the concentration of data allows it without producing artifacts. The current results include both Love and Rayleigh wave inversions across the region for periods from 7 to 100 s on a $1^\circ \times 1^\circ$ grid and at resolutions approaching 1° under some conditions. Short-period group velocities are sensitive to slow velocities associated with large sedimentary features such as the Caspian Sea, West Siberian Platform, Mediterranean Sea, Bay of Bengal, Tarim Basin, and Persian Gulf. Intermediate periods are sensitive to differences in crustal thickness, such as those between oceanic and continental crust or along orogenic zones and continental plateaus. At longer periods, fast velocities are consistently found beneath cratons, while slow upper mantle velocities occur along rift systems, subduction zones, and collision zones such as the Tethys Belt. We have compared the group velocities at various periods with features such as sediment thickness, topographic height, crustal thickness, proximity to plate boundaries, lithospheric age, and lithospheric thickness, and we find significant correlations. We have developed an empirical relationship between long-period group velocity and lithospheric thickness that works well for both oceanic and continental lithosphere. We do not find any similar correlation between the longest-period surface waves and hot spots.

Citation: Pasyanos, M. E. (2005), A variable resolution surface wave dispersion study of Eurasia, North Africa, and surrounding regions, *J. Geophys. Res.*, *110*, B12301, doi:10.1029/2005JB003749.

1. Introduction

[2] Tomographic studies in seismology typically suffer from an uneven distribution of data. This is caused primarily by the concentration of seismic sources within spatially limited regions, outside of which there are large areas that are essentially aseismic. It is also compounded by an uneven distribution of seismic stations due to political and logistical reasons, such as landmass distribution. Regardless of cause, the result is a highly uneven data distribution that strongly samples some regions, while minimally sampling others. One often has to choose between selecting a high-resolution parameterization that likely results in spurious anomalies in low-density regions or to make a lower-resolution model that would not generate this problem. This is generally unsatisfying, as one would like to make the models at as high a resolution as the data permit.

[3] In this study, we have performed a high-resolution surface wave study of Eurasia and North Africa, including areas of the Atlantic, Pacific, Indian, and Arctic oceans (Figure 1). The purpose of this research is to improve maps of fundamental mode surface wave group velocities by enlarging the study region, increasing path density, improving spatial resolution, and expanding the period range. To achieve this, we have implemented a variable smoothing technique to generate group velocity dispersion models of the highest possible resolution. The variable smoothness method produces higher resolution where the data warrant it, and lower resolution outside of the high-density regions.

0148-0227/05/2005JB003749$09.00

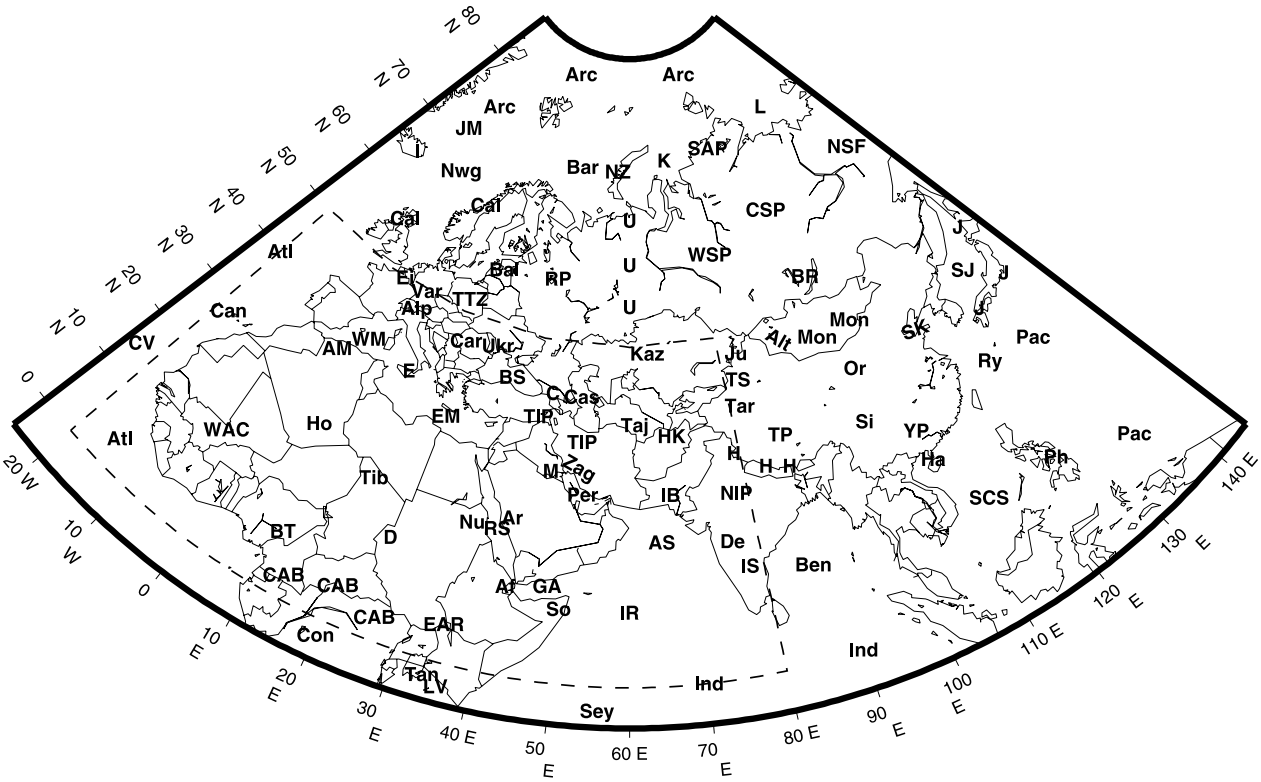

Af=Afar Triple Junction, Alp=Alps, Alt=Altai Mts., Ar=Arabian Shield, AS=Arabian Sea, AM=Atlas Mts, Arc=Arctic Ocean, Atl=Atlantic Ocean, Bal=Baltic Shield, Bar=Barents Sea, Ben=Bay of Bengal, BR=Baikal Rift, BT=Benue Trough, BS=Black Sea, Cal=Caledonides, Can=Canary Is., Car=Carpathians, Cas=Caspian Sea, C=Caucasus, CAB=C.African belt, Con=Congo Craton, CSP=C.Siberian Platform, CV=Cape Verde, D=Darfour, De=Deccan Traps, E=Etna, Ei=Eifel, EAR=E.African rift, EM=E.Mediterranean, GA=Gulf of Aden, H=Himalayas, Ha=Hainan, HK=Hindu Kush, Ho=Hoggar, I=Iceland, Ind=Indian Ocean, IR=Indian Ridge, IS=Indian Shield, IB=Indus Basin, J=Japanese Is., JM=Jan Mayan, Ju=Junggar Basin, K=Kara Sea, Kaz=Kazakh Platform, L=Laptev Sea, LV=Lake Victoria, M=Mesopotamian Foredeep, Mon=Mongolian Platform, NIP=N.Indian Platform, NSF=Northeast Siberian Fold System, Nwg=Norwegian Sea, NZ=Novaya Zemlya, Nu=Nubian Shield, Or=Ordos Basin, Pac=Pacific Ocean, Per=Persian Gulf, Ph=Philippine Is., RS=Red Sea Rift, RP=Russian Platform, Ry=Ryukyu Is., SAP=Siberian Arctic Plain, SCS=S.China Sea, Sey=Seychelles, Si=Sichuan Basin, SJ=Sea of Japan, SK=Sino-Korean Paraplatform, So=Somali Basin, Taj=Tajik Depression, Tan=Tanzania Craton, Tar=Tarim Basin, Tib=Tibesti, TP=Tibetan Plateau, TS=Tien Shan, TTZ=Tornquist-Teisseyre Zone, TIP=Turkish-Iranian Plateau, Ukr=Ukranian Shield, U=Ural Mts, Var=Variscides, WAC=W.African craton, WM=W.Mediterranean, WSP=W.Siberian Platform, YP=Yangtze Paraplatform, Zag=Zagros Mts.

Figure 1. Map of the Eurasia and North Africa region indicating the location of geologic, tectonic and geographic features discussed in the text. Dashed lines demark the area of the previous study by *Pasyanos et al.* [2001].

We are using a very large data set of surface wave group velocity measurements for both Rayleigh and Love waves over a range of periods and determine the lateral variation of surface wave group velocity for each period.

[4] Surface wave dispersion studies have been performed for a number of broad regions including Antarctica [*Ritzwoller et al.*, 2001], Asia [*Yanovskaya and Kozhevnikov*, 2003], Australia [*Debayle and Kennett*, 2000], China [*Huang et al.*, 2003], Eurasia [*Ritzwoller and Levshin*, 1998], and South America [*Vdovin et al.*, 1999] as well as globally [*Ritzwoller et al.*, 2002]. Many more studies exist at smaller regional scales. While this is not the first dispersion model for this region, this model represents a significant improvement in coverage and resolution from any prior studies of the area at this scale. *Ritzwoller and Levshin* [1998] previously performed a top-quality surface wave tomography of a similar area region in Eurasia. They used about 600 events recorded at 83 stations to produce about 9000 paths, resulting in a 5° resolution model. In contrast, this study uses about 12,000 events recorded at some 300 stations to produce dispersion measurements for over 40,000 paths and starting to reach lateral resolutions of 1°.

[5] This paper first presents a discussion of the data and measurements. The next section describes the variable smoothness inversion method and the results of several tests. Finally, the tomography results are presented and systematically compared to parameters indicative of the regional tectonics. There is an excellent agreement between the group velocity maps and tectonic features over a wide range of periods and depths.

[6] It should also be mentioned that several recent publications on surface wave tomography have focused on finite frequency effects [*Spetzler et al.*, 2001, 2002; *Yoshizawa and Kennett*, 2002; *Zhou et al.*, 2004] and one specifically in the case of group velocities [*Ritzwoller et al.*, 2002]. These finite frequency methods each take slightly different approaches to attempt and move beyond ray theory and more closely approximate the true sensitivity kernels. The technique presented here provides an easy to implement method to improve the resolution of surface wave models. It is here applied to basic ray theory

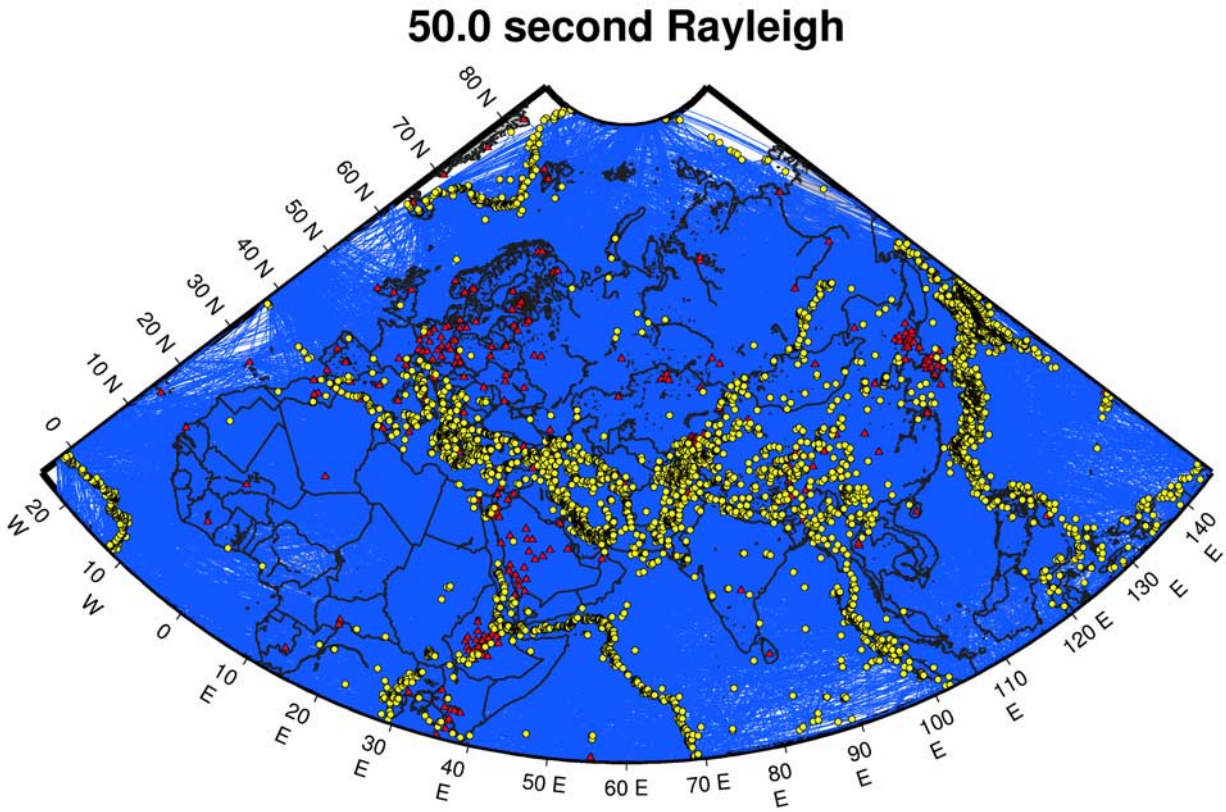

Figure 2. Distribution of earthquakes (circles), stations (triangles), and paths (lines) over the study area for 50 s period Rayleigh waves, illustrating the uneven coverage.

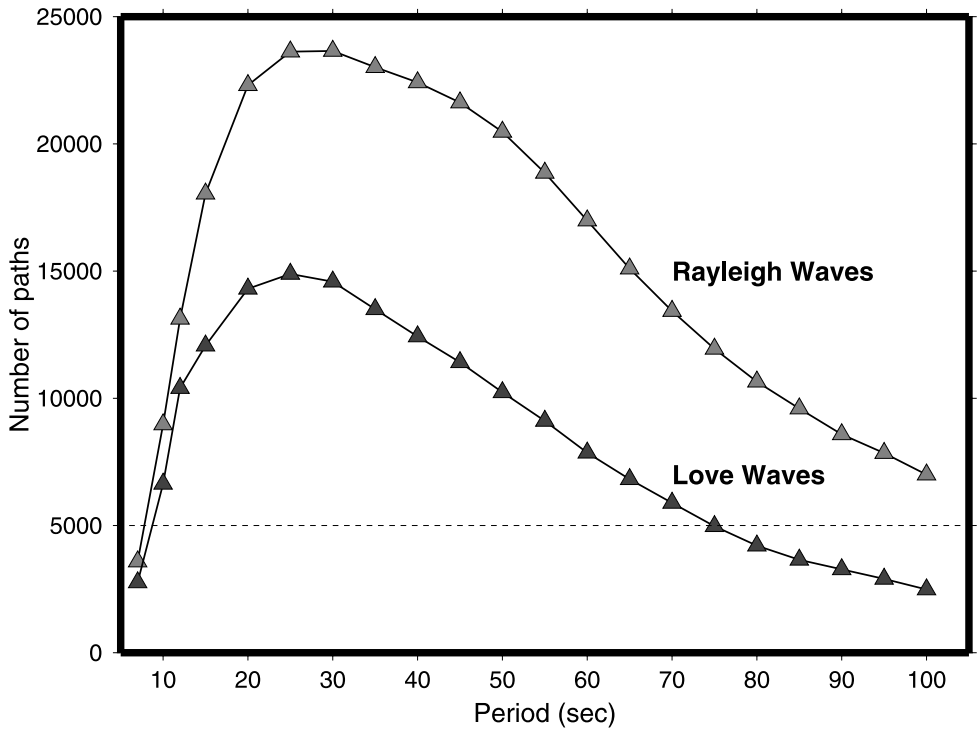

Figure 3. Number of high-quality surface wave measurements made at LLNL (both Rayleigh and Love) as a function of period. The dashed line indicates the level below which the problem is underdetermined.

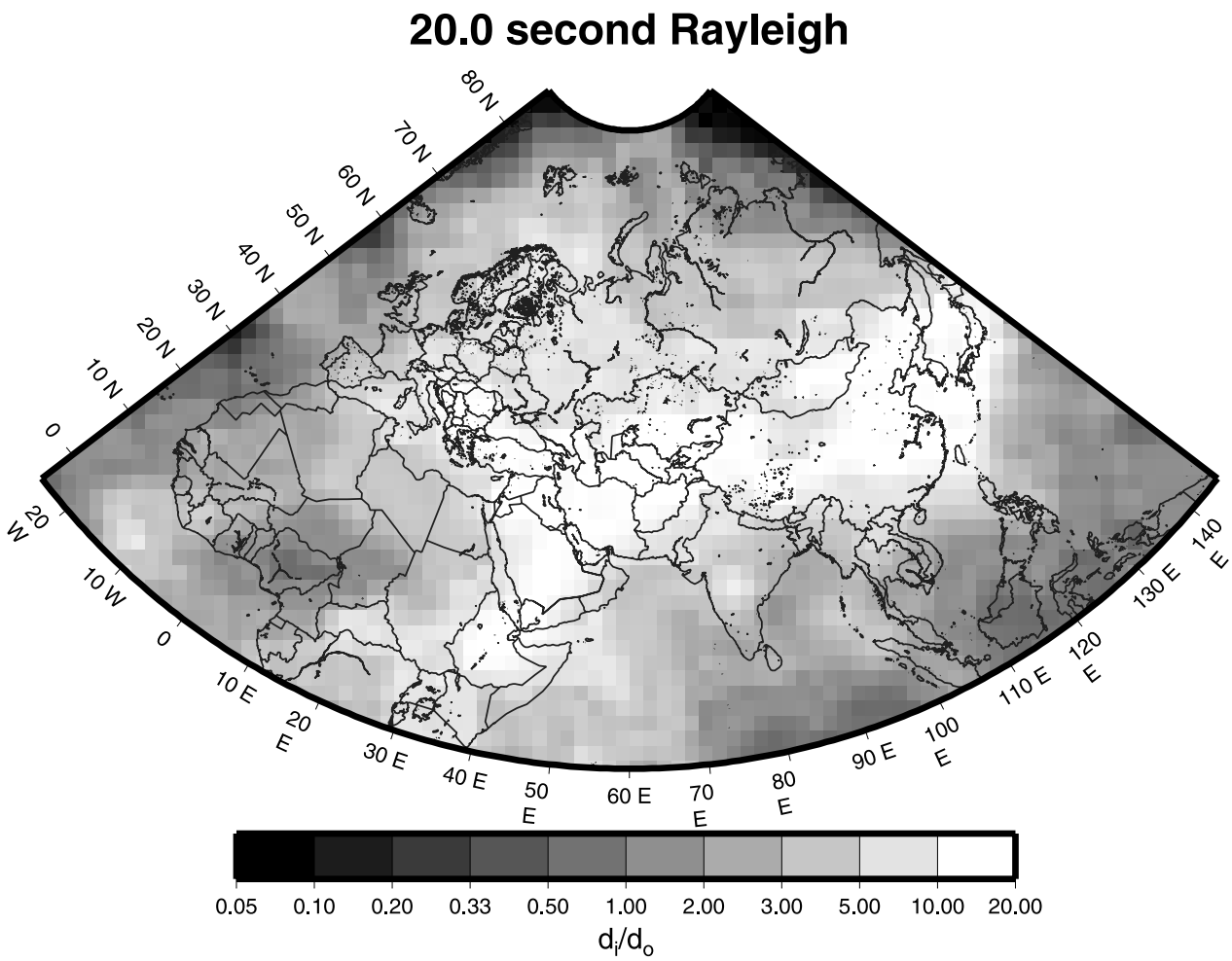

Figure 4. Ratio of individual cell distances to average cell distances (d_i/d_o) for 20 s period Rayleigh waves.

tomography, although it could be as easily applied to finite frequency methods.

2. Data and Measurements

[7] For the surface wave investigation, vertical and transverse component teleseismic and regional seismograms were selected for years 1967–2004. The waveform data were gathered primarily from permanent three-component, digital, broadband stations and supplemented with several portable deployments including PASSCAL experiments in Saudi Arabia, Tanzania, Ethiopia, Kenya, China, and Turkey and several Network of Autonomously Recording Seismographs (NARS) deployments in Europe. Dispersion curves were measured by applying a narrow band Gaussian filter to the broadband displacement seismogram over many different periods [e.g., *Dziewonski et al.*, 1969; *Levshin et al.*, 1972; *Herrmann*, 1973]. Rayleigh waves were measured on the vertical component, while Love waves were measured on data rotated into the transverse direction. The maximum amplitude at each period is picked on the envelope function and the arrival time corresponding to this maximum amplitude is used to compute the group velocity. We use the instantaneous period rather than the filter period to account for any potentially large amplitude variations with frequency. Further information on the details of making the dispersion measurements are described in *Pasyanos et al.* [2001].

[8] In a previous study [*Pasyanos et al.*, 2001], which only covered the portion of our study area south of 50°N latitude and west of 80°E longitude (outlined by the box in Figure 1), 13,500 seismograms were analyzed to determine the individual group velocities of 10–60 s Rayleigh and Love waves. Of these, quality group velocity measurements were made for about 7000 Rayleigh wave and 4000 Love wave paths. Since that study, we have concentrated on making measurements north and east of the previous study in order to expand the tomography into the European Arctic and Asia. To date, we have now examined more than 100,000 seismograms and made quality group velocity

Figure 5. Results using fixed smoothness inversions for 20 s Rayleigh waves with (a) $2° \times 2°$ and $\lambda = 1.0$, (b) $1° \times 1°$ and $\lambda = 2.0$, and (c) the difference between Figures 5a and 5b. The color scheme of Figures 5a and 5b varies from slow (red) to fast (blue).

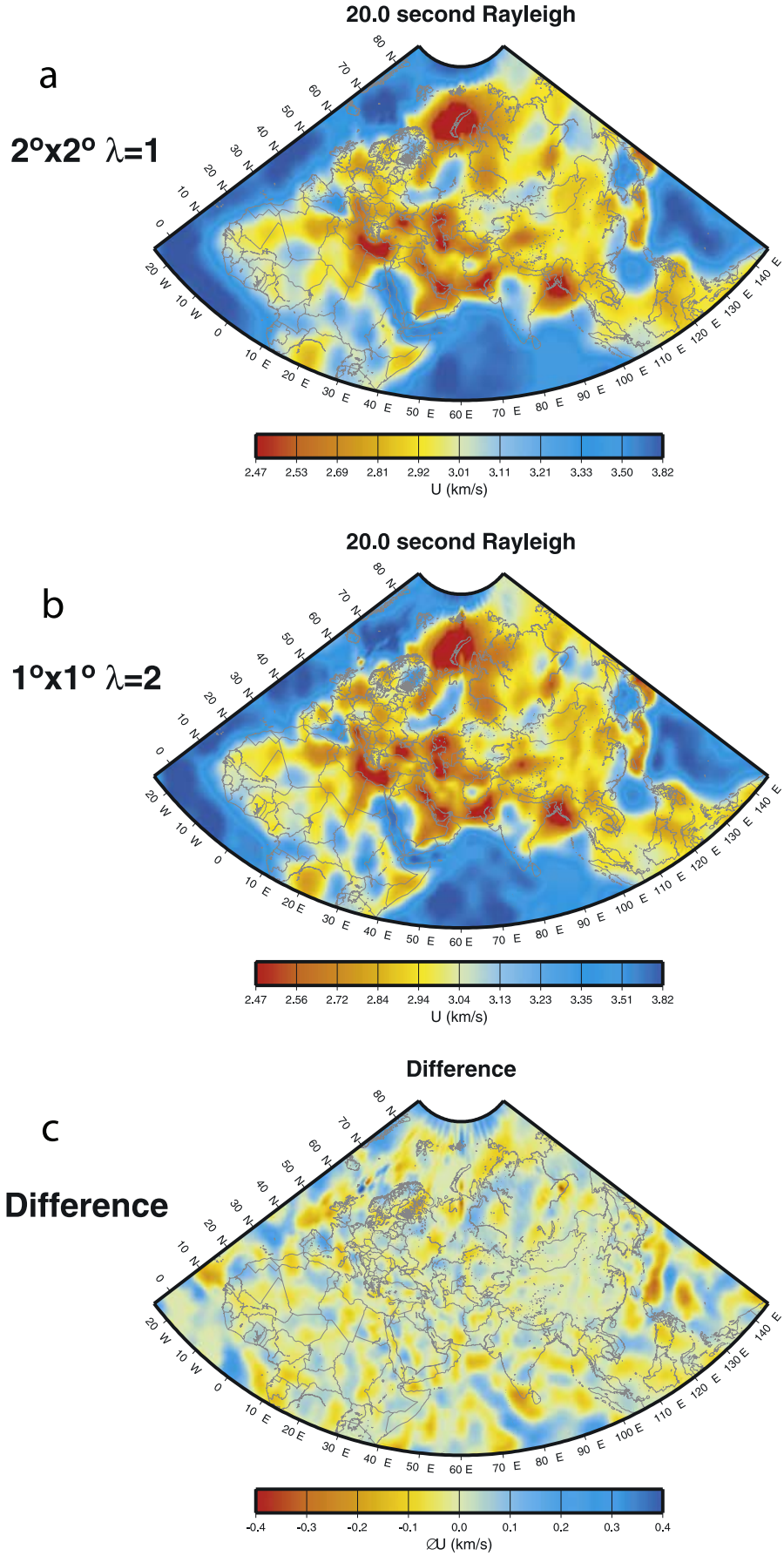
20.0 second Rayleigh
a
2°x2° λ=1
2.47 2.53 2.69 2.81 2.92 3.01 3.11 3.21 3.33 3.50 3.82
U (km/s)
20.0 second Rayleigh
b
1°x1° λ=2
2.47 2.56 2.72 2.84 2.94 3.04 3.13 3.23 3.35 3.51 3.82
U (km/s)
Difference
c
Difference
-0.4 -0.3 -0.2 -0.1 0.0 0.1 0.2 0.3 0.4
∅U (km/s)

Figure 5

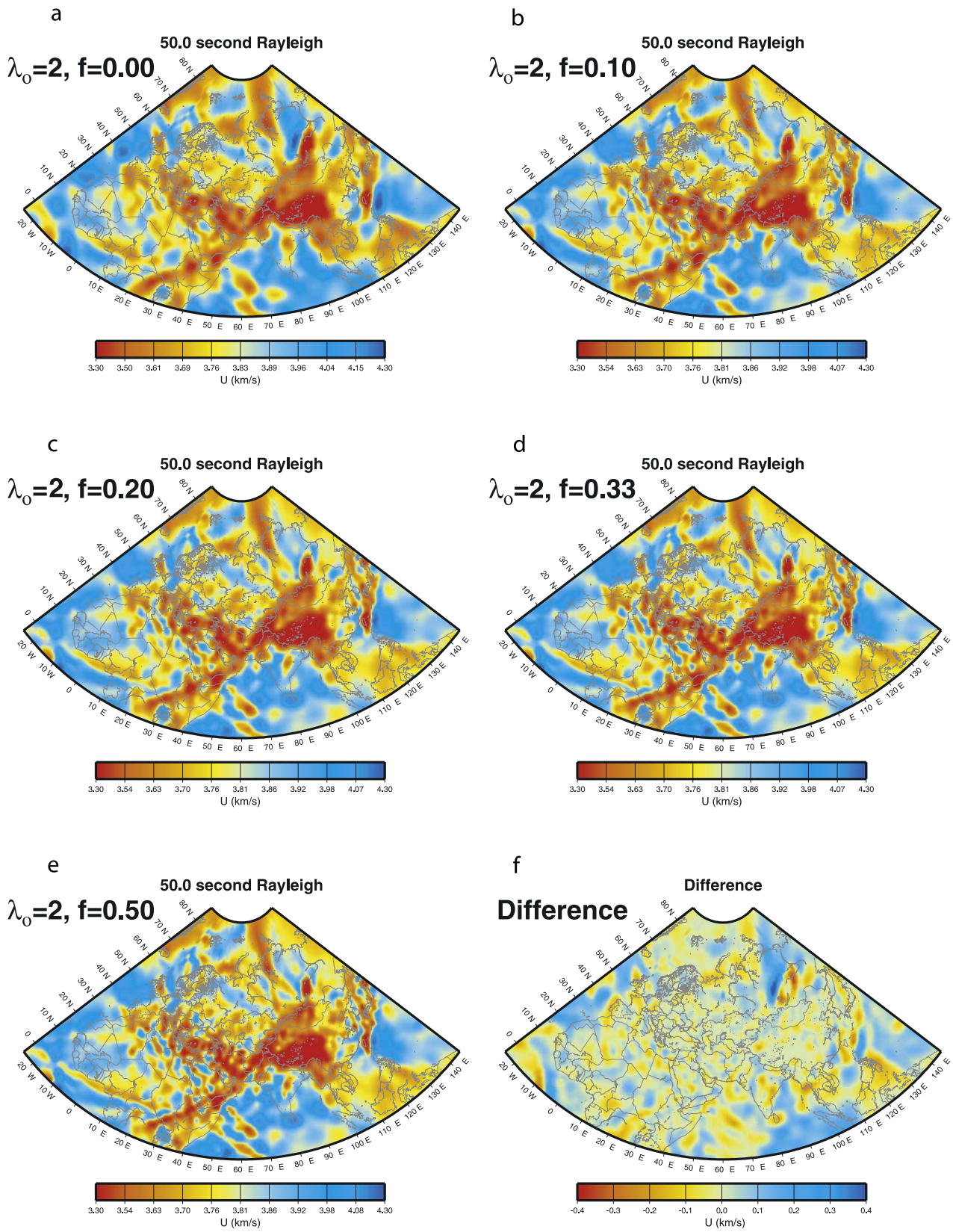

Figure 6. Results using variable smoothness inversions for 20 s Rayleigh waves performed using f factors of (a) 0, (b) 0.1, (c) 0.2, (d) 0.33, and (e) 0.5. (f) Difference between the inversion where $f = 0$ and the inversion where $f = 0.33$. Color scheme is same as in Figure 5.

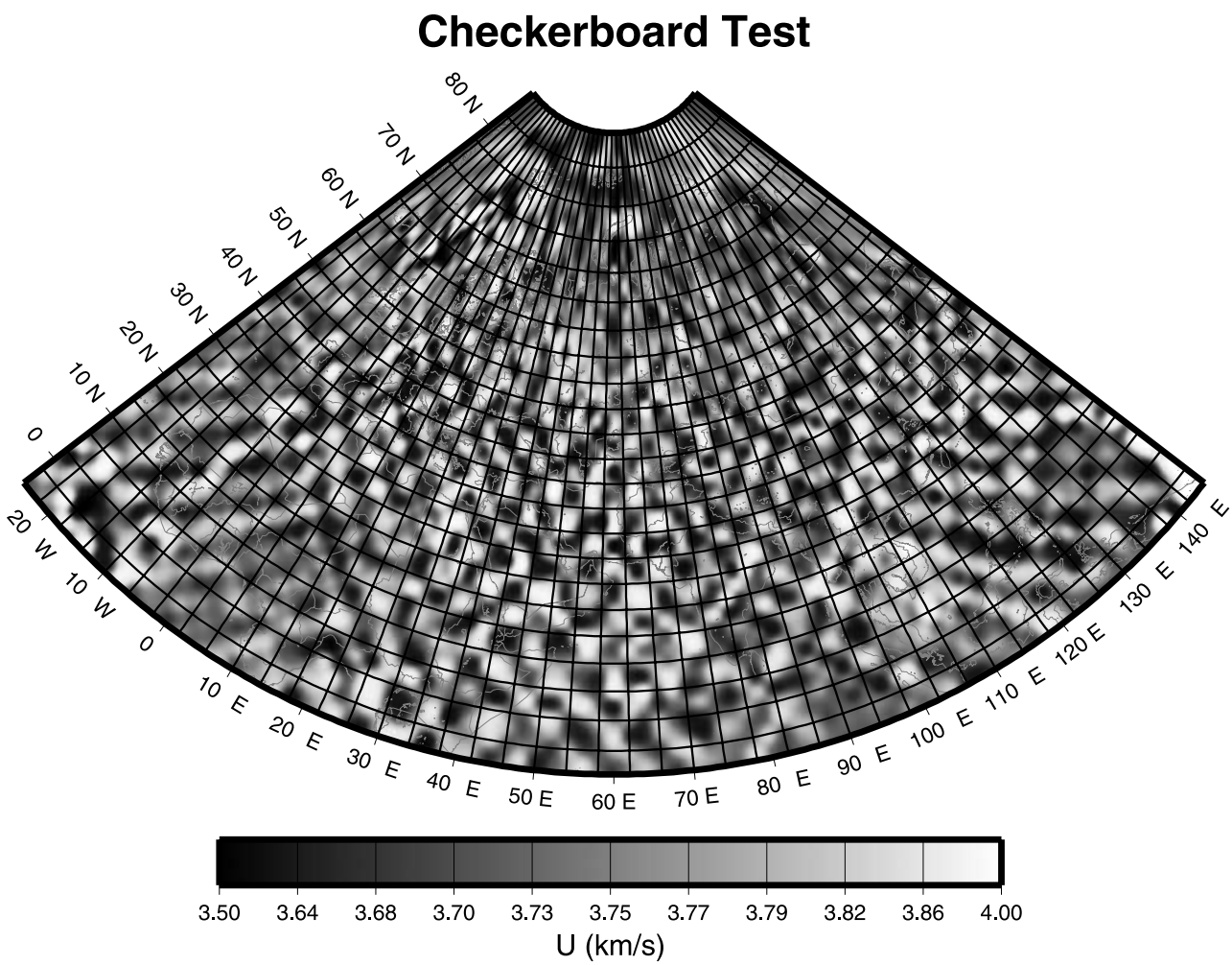

Figure 7. Checkerboard resolution test using path coverage of 50 s Rayleigh waves. The input pattern is a $4^\circ \times 4^\circ$ checkerboard pattern.

measurements for about 30,000 Rayleigh wave and 20,000 Love wave paths. Each path examined makes measurements for multiple periods (the number for each path depending on the signal-to-noise at each filter period). As a result, we have actually made in total some 2.8 million group velocity measurements. In addition, we have incorporated thousands of measurements of researchers from the University of Colorado at Boulder [i.e., *Ritzwoller and Levshin*, 1998; *Levshin et al.*, 2002] who have also made group velocity measurements. These measurements can be confidently combined with our measurements because we have established a consistent measurement procedure [*Walter and Ritzwoller*, 1998].

[9] Figure 2 shows the distribution of earthquakes (circles) and broadband digital seismic stations (triangles) throughout Eurasia and North Africa that are used in this study. Seismicity is concentrated along plate boundaries, mainly the oceanic rifts (Mid-Atlantic Ridge, Indian Ridge), continental rifts (Baikal rift, East African rift, Red Sea), Pacific subduction zones (Philippine Trench, Japanese Trench) and the whole of the Tethys collision zone, spanning from the Atlantic to the Bay of Bengal (see Figure 2). There is also diffuse seismicity throughout central Asia. In contrast, there is almost no seismicity within northern Eurasia, the Indian subcontinent and the rest of the African continent outside of the rift. Instrument coverage is best in Europe and worst in North Africa, India, and oceanic regions. Station coverage is perhaps "overstated" in some regions that had PASSCAL and NARS deployments (Saudi Arabia, Ethiopia, Kenya, Tanzania, northeast China, eastern Turkey, and eastern Europe) as these stations only ran for limited periods of time. Overall, this leads to a highly uneven distribution of surface wave measurements.

[10] An example of path coverage is shown by the map in Figure 2. Paths are densest in regions with seismicity and station coverage and, in general, are lower at the edges of the model. Because of the difficulty in making short-period measurements at long epicentral distances, we have been able to make significantly more measurements at intermediate periods. For example, while there are over 24,000 Lawrence Livermore National Laboratory (LLNL) Rayleigh wave measurements at 30 s, we have only been able to make about 20,000 measurements at 15 s, less than 9000 at 10 s, and only about 4500 at 7 s (Figure 3). The number of group velocity measurements incorporated from other sources ranges from only a few additional paths at the shortest

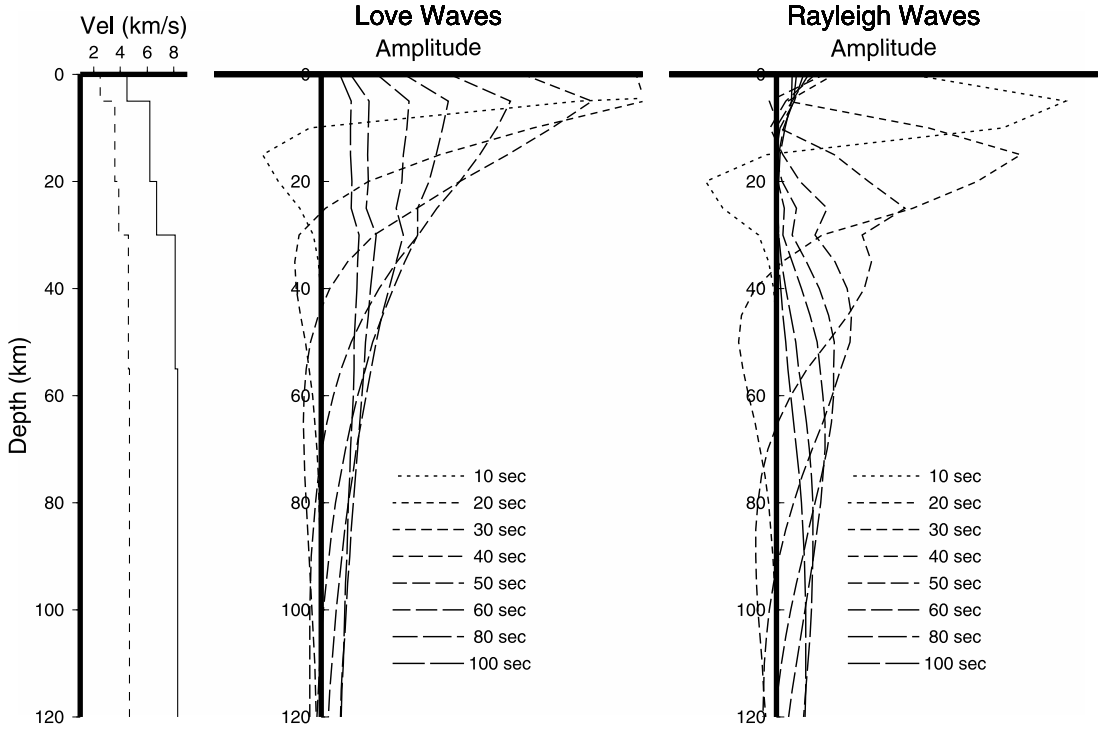

Figure 8. Shear wave (V_s) sensitivity kernels of (middle) Love and (right) Rayleigh waves at periods ranging from 10 to 100 s for a velocity profile that is typical for (left) continental crust. Compressional and shear wave velocity for the model shown as solid and dashed lines, respectively.

periods up to several thousand measurements, in some cases increasing the total number of measurements by about 50%. Because of the poorer signal-to-noise ratio, the number of Love wave measurements is generally less than half the number of Rayleigh wave measurements and is peaked at 25 s period. At 7 s for both Love and Rayleigh waves and for periods greater than 70 s for Love waves, the number of paths falls under 5000. Below this threshold, coverage is spotty and the inversion is underdetermined. This can result in streaky maps and inconsistent group velocities between adjacent periods.

3. Inversion Method

[11] We invert for lateral variations in the surface wave group velocities by gridding the inversion region into equal-area cells and by forming the following system of equations:

$$\mathbf{T} = \mathbf{D}\,\mathbf{S} \tag{1}$$

$$\lambda\mathbf{L}\,\mathbf{S} = \mathbf{0} \tag{2}$$

where **T** is a vector of surface wave group times (distance/group velocity), **D** is a matrix of distances traveled in each cell, and **S** is a vector of group velocity slowness, which is simply the inverse of the group velocity in each cell. In addition to using (1) to fit travel times, (2) imposes a smoothness constraint on the data by constructing the two-dimensional Laplacian operator **L** of the slowness and requiring it to be zero [*Lees and Crosson*, 1989]. The weighting factor λ controls the tradeoff between fitting the travel times and smoothing the model. The weighting of the slownesses in (1) is by distances. In order to have an equal weighting of (2), then λ, though unitless, needs to be roughly similar size. This can be accomplished easily by normalizing the equations either by dividing (1) by an average distance factor or by multiplying (2) by the same factor. We perform the second option, so that when $\lambda = 1$, we are actually weighting by the average distance. When $\lambda = 0$, there is no smoothing, whereas as $\lambda \rightarrow \infty$, the model is completely smooth (i.e., a single velocity for the whole region). This equation imposes a smoothness constraint and damps the travel time inversion. We then solve for **S** in the system of equations using the conjugate gradient method.

[12] The conjugate gradient technique is a search method that works very well on sparse linear systems like the travel time problem. Because there is no matrix inversion involved, it is well suited for large systems of equations. Convergence will theoretically be reached within the number of iterations equal to the number of constraint equations (i.e., number of paths plus number of smoothness constraints). In practice, however, convergence, as determined by both residuals and distances between successive iterations, is very rapid and achieved much sooner. In this study, each inversion runs 30 iterations.

[13] In our previous study [*Pasyanos et al.*, 2001], we explored variations in the values chosen for the weighting

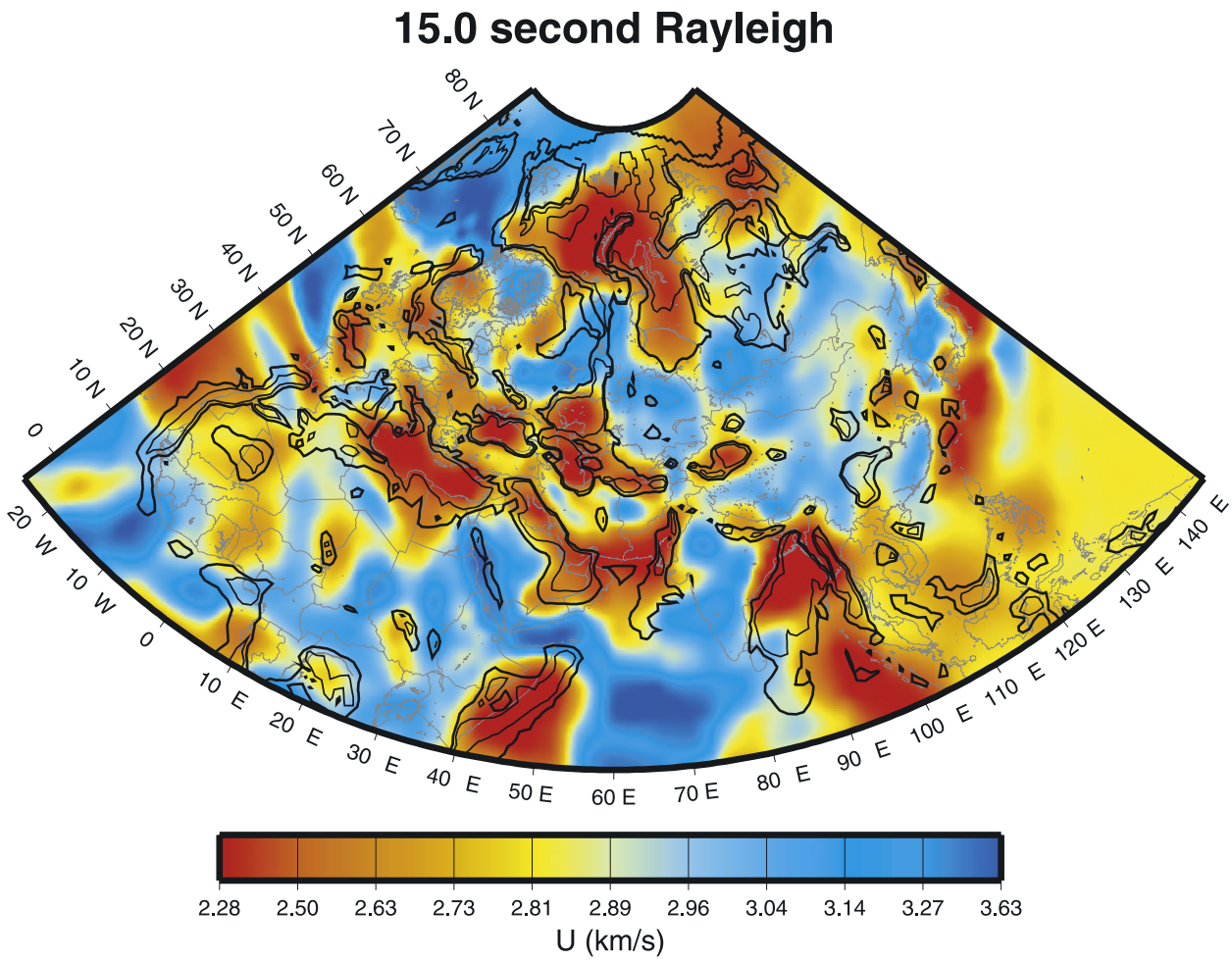

Figure 9. Map of 15 s Rayleigh wave group velocities shown with contours of sedimentary thickness contours (solid lines) for 2.5 km (thicker outer contours) and 5.0 km (thinner inner contours).

factor λ. If the weighting factor is set too low, then the inversion is underdamped and the map exhibits streaking. If the weighting factor is set too high, then the inversion is overdamped and only very broad features will be resolved. When the weighting factor approaches the distances that the paths travel in each cell, then the travel time and smoothness have about equal weights. In all cases, however, we had a value of λ that was constant throughout the region. We wish to explore the spatial variations in this parameter here. The motivation is simple. There is a highly uneven sampling of our region. Where we do not have coverage (aseismic and noninstrumented regions), we would like to have a large effective cell size. This can be accomplished by specifying a high value for λ. Where we do have coverage (seismically active regions and areas with stations), we want to have a small effective cell size, which can be specified by a low value for λ in these regions.

[14] We effect this change by tying local values of λ to path density within a cell. We can achieve this in any number of ways. The method selected compares the total distance of rays traveling within a cell (specified by d_i) to d_o, the average distance traveled within all of the cells (simply the sum of all path lengths divided by the number of cells). An example map of these ratios is shown in Figure 4. This ratio is then used to change the value of the damping parameter (with the average weighting factor value for the model given as λ_o).

$$\lambda_i = \lambda_o \left[\frac{d_o}{d_i}\right]^f \tag{3}$$

[15] We modulate the strength of this variation by a factor f for the power law. If f is 1, then values of λ would simply be directly proportional to the ratio of cell density. Since some regions (like those containing seismic stations) are sampled more than 35 times greater than the average, this would result in extremely large variations in the damping factor. A value of f of 1/2 provides a square-root power law, a value of 1/3 a cube-root power law, etc. If f is set to 0, then we are simply left with a uniform value of λ in our inversion. For practical reasons, we specify a maximum value of λ, so that this value does not blow up if we have cells without any data at all.

[16] The first test that we perform on the inversion method is to compare the results that we get by varying grid size and the parameter λ. Figure 5a shows the results of inverting 20 s Rayleigh wave group velocities with a grid

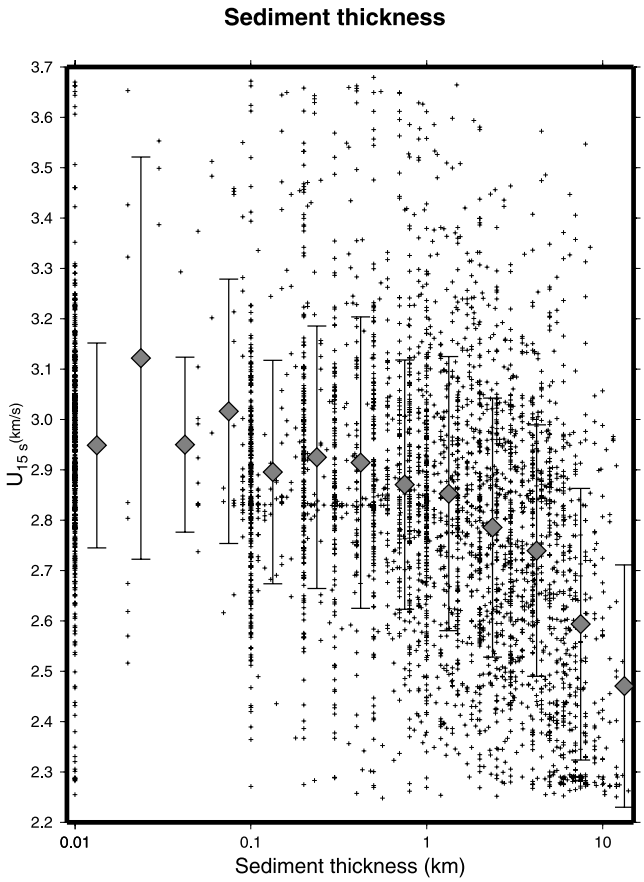

Figure 10. Correlation between 15 s Rayleigh wave group velocities (in km s^{-1}) and sediment thickness (in km). The x axis is shown in logarithmic scale. Diamonds and bars indicate the mean and standard deviation of group velocity values in that sediment thickness range.

size of 2° and λ fixed at 1. This is equivalent to the tomographic inversions performed in our previous study [*Pasyanos et al.*, 2001]. The middle panel shows the results when the grid size has been reduced to 1°, but λ is increased to 2, making the effective grid size about the same as the previous inversion. The inversion results are nearly identical (as shown by the difference plotted in Figure 5c), which is the outcome that we would expect. The allowable resolution of the model can be reduced without changing the results as long as we can compensate by increasing the damping accordingly. This would not be something one would normally choose to do since reducing the grid size increases the inversion time without any corresponding benefit in increased resolution. With this result, however, we can now start to experiment with variations in the smoothing parameter.

[17] In the next test, we are interested in finding out what level of variation in parameter λ is appropriate. The variable inversion method is used to invert 50 s Rayleigh waves, where the grid size is kept at 1° but λ is now allowed to vary according to (3). As mentioned previously, we typically see variations in path density ranging from 0 to about 30 times the average density. Values in the parameter f of 0, 0.1, 0.2, 0.33, and 0.5 would result in maximum reductions in λ of about 1, 1.5, 2, 3, and 6, respectively, and typical overall variations in λ about double that. Results are shown in Figure 6. As f is increased, one can see the natural progression that is expected. Many features narrow when the variation is increased. At the same time, however, we see what appears to be spottiness and streaking which is smoothed in the less variable models. Visually, it appears that the model is clearly underdamped when f = 0.5, and still underdamped when f = 0.33. The difference between f = 0 (no variations) and f = 0.33 is shown in the final panel. The most significant changes occur in Siberia. More specifically, the low-velocity feature along the Baikal Rift narrows considerably, and the high-velocity feature to the west of Baikal (which compensates the slow Baikal velocity along many paths) almost completely disappears. Also, there are some minor differences in the central Atlantic and around the Philippine Islands and Philippine Plate. These appear to be due to minor shifts in the boundaries between high- and low-velocity anomalies. For the purposes of this study, we have selected an f factor of 0.20 for all inversions. Parameter λ_o, on the other hand, ranges from 2 to 5 for Rayleigh waves and from 2 to 10 for Love waves, with the largest damping factors at short periods (7 s) and long periods (>80 s).

[18] In the final test, we estimate spatial resolution by performing a checkerboard test for the region. We use a 4° × 4° checker pattern which, because the study area spans a large latitude range, actually becomes significantly thinner to the north. Results of the tomographic inversion are shown in Figure 7. What we find is basically what we would expect from the path density (Figure 4). There is good resolution in the Mediterranean, North Africa, East Africa, Europe, the Middle East, central Asia, China, and western Indian Ocean. There is poorer resolution in central Africa, the Mid-Atlantic Ocean, northern Eurasia, Siberia, and Indonesia.

4. Results

[19] This section presents the results of the group velocity inversions performed using the method described in section 3. We first describe the Rayleigh wave maps over a range of periods, along with a discussion of regional tectonics. This is then followed by a shorter discussion of the Love wave maps. Group velocity maps for both Love waves (Figures S1 and S2) and Rayleigh waves (Figures S3 and S4) at all periods are provided in the auxiliary material[1]. Lateral group velocity variations, as measured by the 2σ standard deviation, range from 10 to 20%, with larger variations occurring at shorter periods. The maps are well resolved in regions with many crossing paths (see Figure 2), such as northeast Africa, the Mediterranean Sea, Europe, the Middle East, Arabian Peninsula, central Asia, East Asia, and most of the Indian subcontinent. Results from the far northern Arctic, west Africa, eastern Siberia, Indonesia, and parts of the Atlantic and Indian oceans, which have low path density and correspondingly higher values of λ, should be taken with the appropriate

[1] Auxiliary material is available at ftp://ftp.agu.org/apend/jb/2005JB003749.

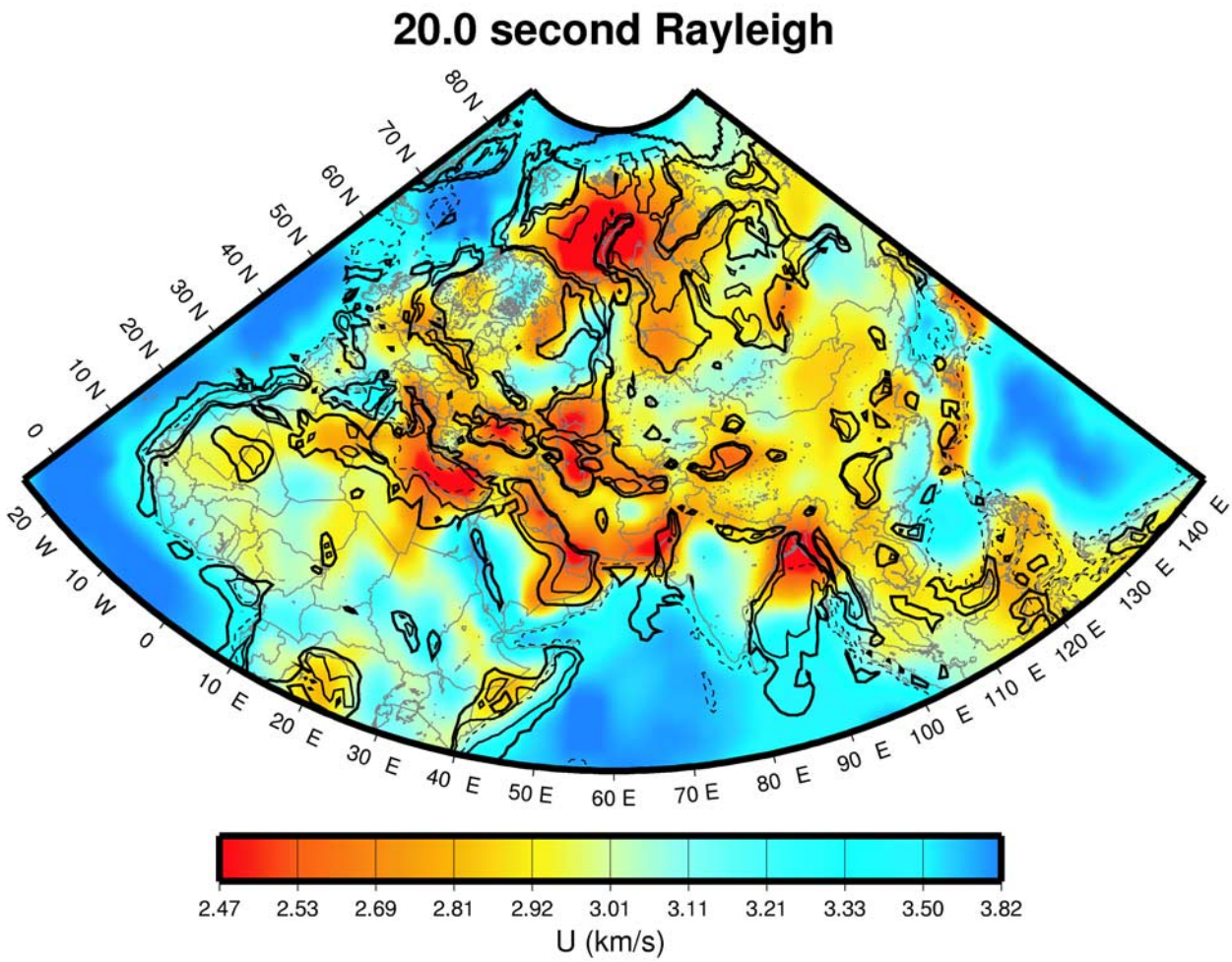

Figure 11. Map of 20 s Rayleigh wave group velocities shown with sediment thickness contours (solid lines) and boundary between oceanic and continental crust (dashed lines).

precautions. One notable feature in both the Rayleigh and Love wave maps is that there is generally very good continuity between adjacent periods. Since each period is inverted completely independently and contains different sets of measurements, this suggests that the anomalies are true structural features, rather than random noise, although it is still possible that there may be systematic errors in the group velocity measurements.

[20] Figure 8 shows characteristic velocity sensitivity kernels of different period Love and Rayleigh waves. Since the kernels depend on the velocity structure, these particular curves are meant to illustrate the sensitivity of them to typical continental crust, in this case one with a sediment thickness of 5 km and a crustal thickness of 30 km. The Love wave sensitivity kernels are shaped like exponential functions, while the Rayleigh wave sensitivity kernels are more Gaussian. At longer periods, the Love wave sensitivity kernels continue to be sensitive to shallow structure and are simply flatter and less peaked. In contrast, the Rayleigh wave sensitivity kernels are peaked at deeper depths for increasing periods (i.e., ~10 km at 10 s, ~20 km at 20 s, etc.). We now wish to try and correlate the group velocity map with tectonic features of our study area. Because of the shape of the sensitivity kernels, we make comparisons to Rayleigh waves, which are better able to isolate the anomalies with depth features.

[21] There is excellent correlation between short-period group velocities and sediment thickness. Sediments having significantly slower shear wave velocities than crystalline crust, regions with thick sedimentary basins have markedly slower surface wave group velocities. Figure 9 shows a map of 15 s Rayleigh waves (primarily sensitive to shear velocity in the upper 15 km) shown with contours of sedimentary basins with sediment thickness greater than 2.5 and 5.0 km. Contours are derived from the Laske sediment thickness model [*Laske and Masters*, 1997]. There is significant correspondence between the two for the largest and deepest basins such as the Eastern Mediterranean, Persian Gulf, Mesopotamian Foredeep, Black Sea, Caspian Sea, Indus Basin, Russian Platform, Barents Sea, Bay of Bengal, Tarim Basin, west Siberian, and Somali basins. This relationship is somewhat muddled where the sedimentary basins are located in or extend into ocean crust, such as the Red Sea, Western Mediterranean, and Bay of Bengal. There is also a surprisingly good match with many of the smaller basins

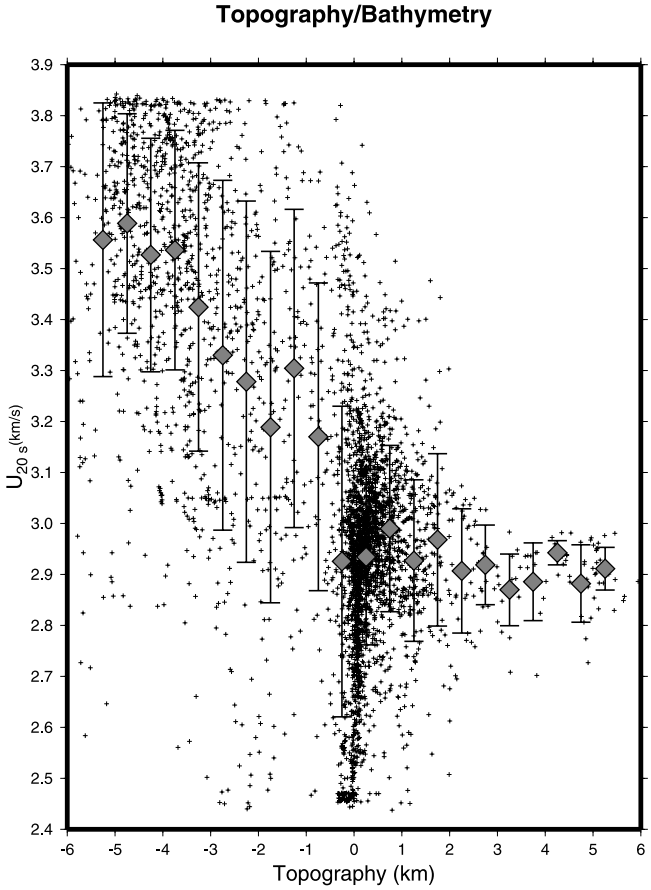

Figure 12. Correlation between 20 s Rayleigh wave group velocities (in km s^{-1}) and topography/bathymetry (in km). Diamonds and bars indicate the mean and standard deviation of group velocity values in that topography range.

like those in North Africa and Europe, indicating the high resolution of the maps. One notable exception seems to be the Central Siberian Platform, which does not appear to be well resolved, probably due to poor coverage of this region at short periods. An area of disagreement in a well-resolved region is the area around the Gulf of Oman, Arabian Sea, and southern Iran and Pakistan, where we require significantly thicker sediments. *Clift and Gaedicke* [2002] find that sediment thickness in the region approaches 12 km, significantly deeper than the thickness found in the sediment model. Figure 10 shows a correlation between 15 s group velocities and sediment thickness. The diamonds and bars show the average and standard deviation in each sediment thickness range. While the scatter in these features is high, there is a clear trend between the two quantities, indicating over a 0.5 km s^{-1} (15–20%) difference between regions of thinnest and thickest sediments.

[22] As we move to slightly longer periods (~20 s), we find that we are still sensitive to sedimentary basins (particularly the deepest basins) but that there is an extremely strong correspondence between the group velocities and differences between oceanic and continental crust. In this case, oceanic crust is so considerably thinner than continental crust (5–10 km instead of 30–40 km) that even by the relatively short period of 20 s (which is primarily sensitive to depths between 10 and 30 km), the surface waves are sensing the upper mantle in the oceans. Since mantle shear wave velocities are significantly faster than crustal shear wave velocities (~4.5 km s^{-1} instead of ~3.0 km s^{-1}), oceanic lithosphere will have faster group velocities. Figure 11 shows a map of 20 s Rayleigh wave group velocities. We have kept the sediment thickness contours (shown in solid lines) but have also added lines which approximate the boundary between oceanic and continental crust (shown in dashed lines). This line along the continental slope has been created by taking the 500 m bathymetry contour from ETOPO5 [*National Geophysical Data Center*, 1998]. Contours taken at 1000 m and 1500 m would not be significantly different. Slightly slower group velocities are still found in the sedimentary basins; however, the slowest velocities are only found in the deepest basins (Eastern Mediterranean, Black Sea, Caspian Sea, Indus Basin, Persian Gulf, Barents Sea, Bay of Bengal). For example, in the Mediterranean Sea, the slow velocities are limited to a smaller region at 20 s than at 15 s, corresponding to the region with the deepest sediments (~10 km). The most significant feature of these maps is the rapid transition in group velocities at the interface between continental and oceanic crust. For instance, in the northern part of the study area, the transition from slow to fast group velocity occurs not at the shoreline, nor at the basin edge but at the continental slope which includes the Barents Sea, Kara Sea, and Laptev Sea in the continental region. The Gulf of Aden, Western Mediterranean, Sea of Japan, and Red Sea have fast velocities, consistent with their near-oceanic crustal thicknesses. Figure 12 shows the correlation between topography/bathymetry and 20 s Rayleigh wave group velocity. What is most obvious is the dichotomy between oceanic and continental crust, with significant variations within each group. In particular, within oceanic crust, there is a very striking trend between group velocity and bathymetry. This feature may be caused by the cooling of oceanic lithosphere, which causes the deepening of the bathymetry with age. There does not appear to be any significant trend between topographically high (and presumably also thick crust) regions.

[23] At intermediate periods (30–40 s), we find that the group velocities are primarily sensitive to crustal thickness, not only between oceanic and continental crust, but also between continental crust of varying thickness. Again, in areas of thick crust, intermediate-period surface waves will be slower because crustal shear wave velocities are so much slower than mantle velocities. Figure 13 shows a map of 40 s Rayleigh wave group velocities plotted with a few contours of crustal thickness (shown in solid lines) and 500 m bathymetry contours continue to be shown in dashed lines. The crustal thickness contours have been derived from the CRUST2.0 model [*Bassin et al.*, 2000] and are shown for 45, 55, and 65 km levels. Obviously, the most significant match is in the Himalaya Mountains and Tibetan plateau where the crust is thickest and the group velocities are the slowest. There is also correlation with orogenic zones like the Zagros Mountains, Hindu Kush, and Caucasus. In other areas (i.e., Baltic Shield, Ural Mountains), the correlation appears to be weaker.

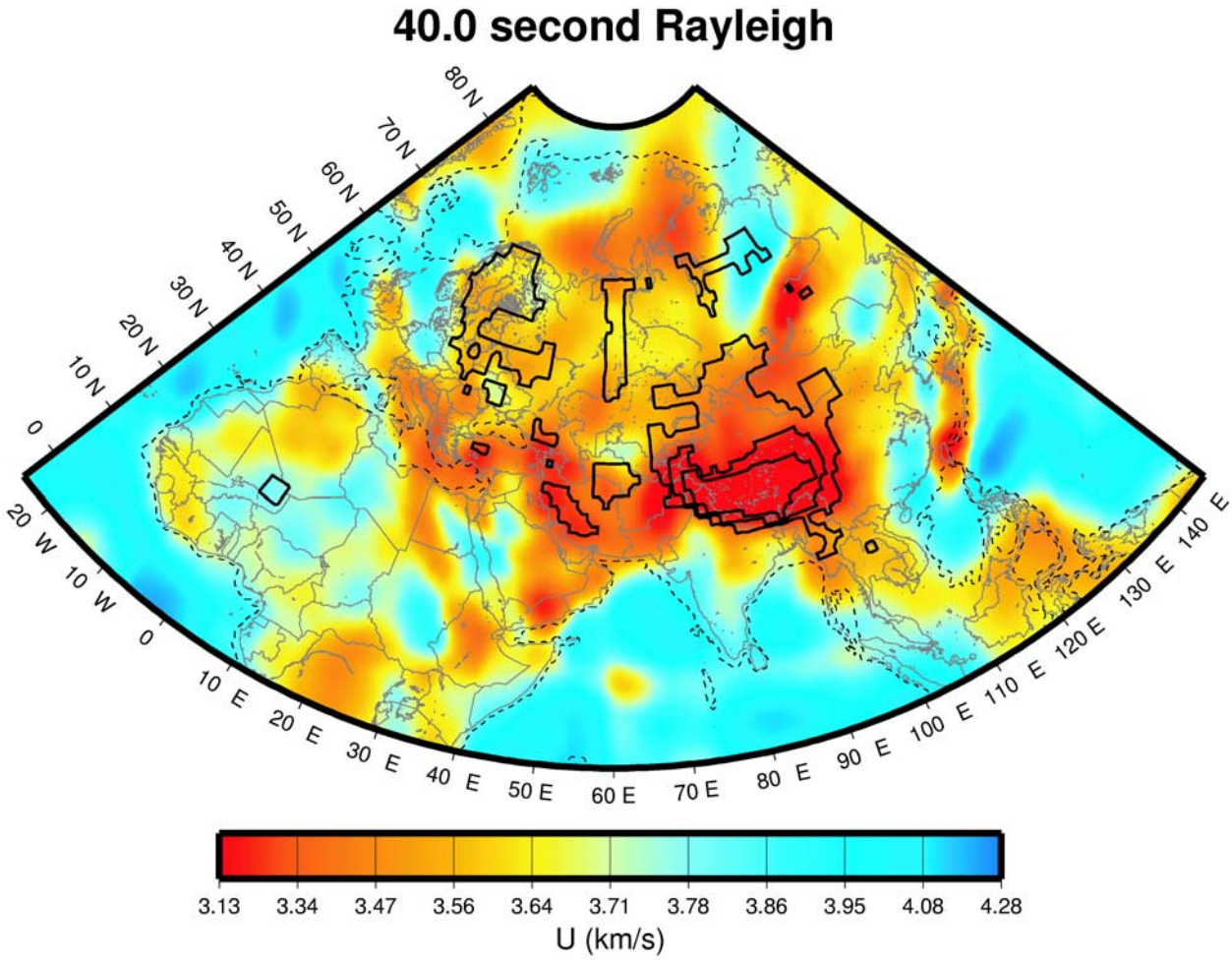

Figure 13. Map of 40 s Rayleigh wave group velocities shown with crustal thickness contours of 45, 55, and 65 km (solid lines) and boundary between oceanic and continental crust (dashed lines).

This is probably due to variations in the shear wave velocity in both the crust and upper mantle. For example, in active orogenic zones, thick crust is often coupled with slower felsic crust and slower upper mantle velocities, while the same features might not be found in other regions (such as shields and older orogenic zones) having thick crust [i.e., *Rudnick and Fountain*, 1995; *Mooney et al.*, 1998]. Figure 14 shows the correlation between crustal thickness and 40 s group velocities. There is a very strong correlation between the two values over the whole range of values, resulting in a difference of 0.4 km s^{-1} (or almost 10% variation) between oceanic crust (<10 km thick crust) and "typical" continental crust (30–40 km thick) and another 0.4 km s^{-1} difference for the thickest crust. There are some indications from Figure 14 that CRUST2.0 may be underestimating crustal thickness at the upper end of the scale in Tibet. There is, in fact, some evidence that the region could have very thick crust over a wider extent [e.g., *Herquel et al.*, 1995] and the Moho could be even deeper in the regions with some of the thickest crust [e.g., *Yuan et al.*, 1997]. It also appears that there is significantly more variation in crustal thickness in Africa than the variation found in CRUST2.0, which has an almost constant crustal thickness of 40 km across the continent.

[24] By 60 s, except in regions with the thickest crust like Tibet, the sensitivity kernels are almost exclusively sensitive to the shear wave velocities in the uppermost mantle. Simply put, where upper mantle velocities are slow, the group velocities are slow, and where the upper mantle velocities are fast, the group velocities are fast, with only a limited influence from the crust. Figure 15 shows a map of 60 s surface waves with the (45, 55, and 65 km) crustal thickness contours from the previous map displayed, along with the addition of plate boundaries. The boundaries shown are from the compilation of *Coffin et al.* [1998]. In addition to the slow group velocities from Tibet, there is a strong relationship between slow group velocities and plate boundaries. This correspondence seems to exist for all types of plate boundaries: oceanic rifts (Mid-Atlantic rift, west Indian rift, Arctic rift, Gulf of Aden), continental rifts (East African rift, Red Sea rift, Baikal rift) and convergent orogenic zones (East Pacific subduction zone, Tethys collision zone along the Alpine-Himalayan belt). In the rift zones, slow upper mantle velocities are the result of hotter, upwelling mantle material, and thinned lithosphere. In

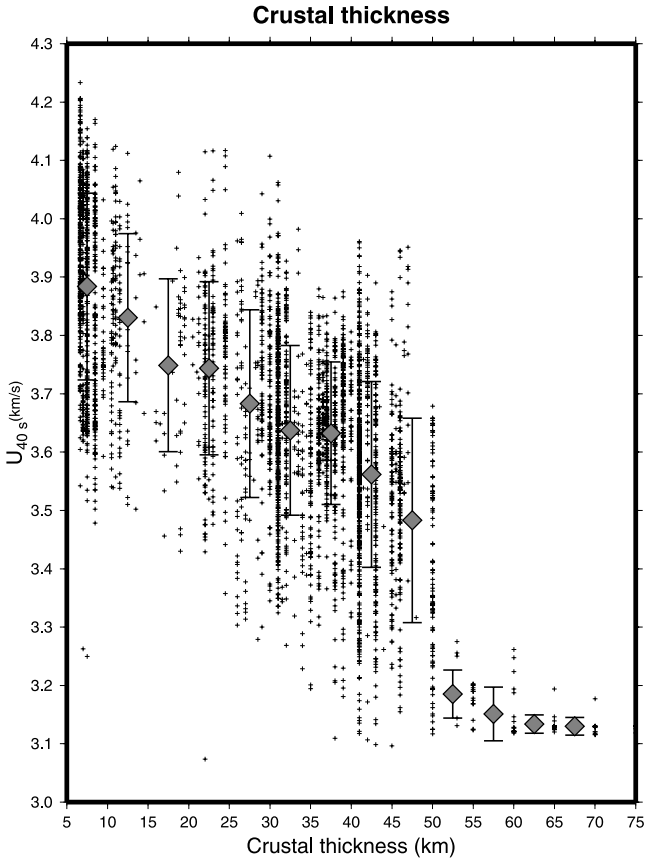

Figure 14. Correlation between 40 s Rayleigh wave group velocities (in km s^{-1}) and crustal thickness (in km). Diamonds and bars indicate the mean and standard deviation of group velocity values in that crustal thickness range.

convergence zones, slow velocities are probably related to the process of recent convective rejuvenation of the upper mantle [e.g., *Houseman and Molnar*, 2001] or caused by the slow, volatile rich material in the wedge above the subducting slab [e.g., *Wiens and Smith*, 2003]. Here, we have correlated 60 s Rayleigh waves with proximity to a plate boundary, determined by calculating the nearest plate boundary point (Figure 16). At distances farther than 10°, we do not see any effect. At shorter distances, however, there is a strong effect to slower velocities, to the tune of about 0.2 km s^{-1} over 10°, a significant 5% variation at these periods.

[25] Long-period (>70 s) group velocities are sensitive to structures even deeper in the upper mantle, with peak sensitivity deeper than 100 km. One would expect hot, upwelling material to have slow group velocities at these periods, while cold material should be fast. Figure 17 shows a map of 80 s group velocities with plate boundaries (solid lines), hot spots (crosses and triangles), and the boundaries of stable platforms and Archaean cratons (single and double hatched lines, respectively). Hot spots are from the compilation of *Sleep* [1990] and are scaled according to buoyancy flux, while the regionalization was derived from the 3SMAC model [*Nataf and Ricard*, 1996]. At this period, we continue to see slow velocities associated with plate boundaries. At these longer periods, however, the velocities in rift zones (i.e., Mid-Atlantic Ridge, Afar) are slower than in convergence zones, indicating that the slow material is deeper in rifts. This is consistent with our understanding of where the slow material in convergence zones comes from, that is, from the relatively shallow wedge above the subducting slab. The slow material in the rifts appears to be deeper seated. A significant correspondence can also be found between fast velocities and older crust. For example, while it appears that orogenic zones are slow, stable continental areas (including the West African Shield, Congo Craton, Baltic Shield, Russian Platform, Central Siberian Shield, Indian Shield, and Yangtze Platform) are fast. These older areas are underlain by thick, cold, fast lithospheric material. One notable exception seems to be the Sino-Korean Paraplatform, which has had its lithospheric mantle more recently affected by nearby subduction [*Griffin et al.*, 1998]. Another exception is in the Benue Trough in Cameroon, which is the remnant of a failed rift system. Figure 18 shows the correlation between crustal age and 80 s Rayleigh wave group velocities. The ages of oceanic crust were derived from *Muller et al.* [1997]. Continental ages were taken from the regionalization by *Nataf and Ricard* [1996], which were themselves based upon the map of *Sclater et al.* [1980], and are plotted as ranges. We see a clear trend within both groups. Within the ocean crust group, however, we find increasing velocities only up until 70 Ma, when the trend flattens and reverses slightly. This appears to be consistent with the reheating phase of the Pacific described by *Ritzwoller et al.* [2004], although our data are not sufficient at long ages to observe a second cooling phase.

[26] Figure 19 shows the correlation of the 80 s group velocities with lithospheric thickness. The thicknesses of the continents were derived from the 1300°C isocontour from *Artemieva and Mooney* [2001], which is modeled based on an inversion of the global compilation of heat flow data. The thicknesses of the oceanic lithosphere are derived from the oceanic age according to the well-known formula:

$$z = 2.32\sqrt{\kappa t} \tag{4}$$

where $\kappa = 1.0^{-6}$ m^2 s^{-1} [*Turcotte and Schubert*, 1982]. Deviations from this model at large ages, particularly for seafloor depth, have been well-documented [*Parsons and Sclater*, 1997; *Stein and Stein*, 1992]. The correlations here are quite significant, with older, thicker lithosphere about 0.5 km s^{-1} faster than a younger, thinner one. On the basis of Figure 19, we have developed an empirical relationship between long-period group velocity and lithospheric thickness. If we regress against the y axis (making lithospheric thickness a function of group velocity), we find that the lithospheric thickness (km) is related to the group velocity (km s^{-1}) by

$$z_{\text{litho}} = 500[\max(U, 3.7) - 3.6] \pm 40 \tag{5}$$

In regions where the group velocities are faster than 3.7 km s^{-1}, the regression finds the lithospheric

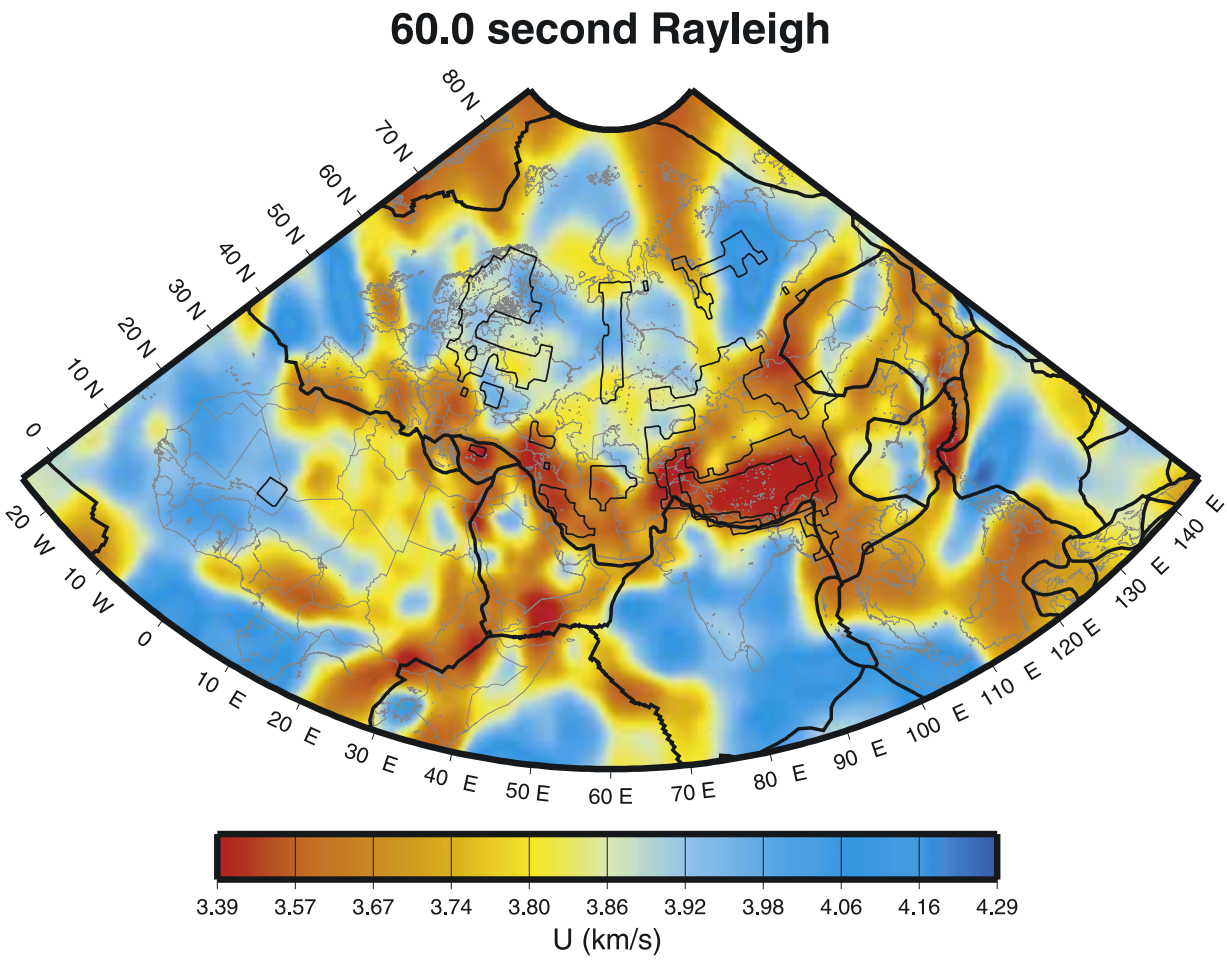

Figure 15. Map of 60 s Rayleigh wave group velocities shown with crustal thickness contours (solid lines) and plate boundaries (thick lines).

thicknesses linearly increasing. In regions with velocities slower than 3.7 km s^{-1}, we find the lithospheric thicknesses to be less than 100 km, regardless of velocity. The formula works well for both oceanic and continental lithosphere, providing a quick estimate when no other information on lithospheric structure might be available.

[27] Visually, there does not seem to be any significant connection between slow long-period group velocities and hot spots, other than those hot spots that coincide with plate boundaries (i.e., Afar, Iceland, Jan Mayan Island). When we look at the correlation between 80 s Rayleigh waves and distance to the nearest hot spot (Figure 20), there is only a weak correlation of ~0.1 km s^{-1} over 15° (primarily dominated by the plate boundary hot spots), after which other factors dominate. Maps at even longer periods (>80 s) are similarly uncorrelated. This perhaps is due to the relatively small spatial extent of these anomalies [*Montelli et al.*, 2004], which cannot be effectively imaged by long-wavelength surface waves. Alternatively, this could be due to the lack of an existing anomaly below the lithosphere, as suggested by a number of researchers [*King and Anderson*, 1995; *Anderson*, 1996]. The hot spots where we do see the largest negative velocity anomaly at long periods coincide with the list of transition zone hot spots from the study of *Ritsema and Allen* [2003].

[28] Figure 21 shows the Love wave maps for the same set of periods. Because of their sensitivity to shallow structure, Love waves show somewhat similar features to the short-period Rayleigh waves. In general, however, the resolution of the Love waves is poorer than that of the Rayleigh waves, most likely attributable to the fewer number of measurements and the lower signal-to-noise ratio of the data. The Love waves also look fairly similar over a wide range of frequencies due to the continuing sensitivity of the Love waves to shallow surface structure at longer periods (see Figure 8). Love waves between 10 and 20 s highlight shallow sedimentary basins (Figures 21a and 21b). Between 25 and 40 s, slow group velocities are limited to the deepest basins. Slow velocities are found in the Eastern Mediterranean, Persian Gulf, Black Sea, Caspian Sea, Somali Basin, Bay of Bengal, Tarim Basin, West Siberian Platform, and the continental shelf north of Russia. We find fast velocities in the ocean basins at these periods.

[29] We only start to see sensitivity to crustal thickness for Love waves at longer periods (40–60 s) than the Rayleigh waves (Figures 21c, 21d, and 21e), where we find slow velocities associated with the Zagros Mountains,

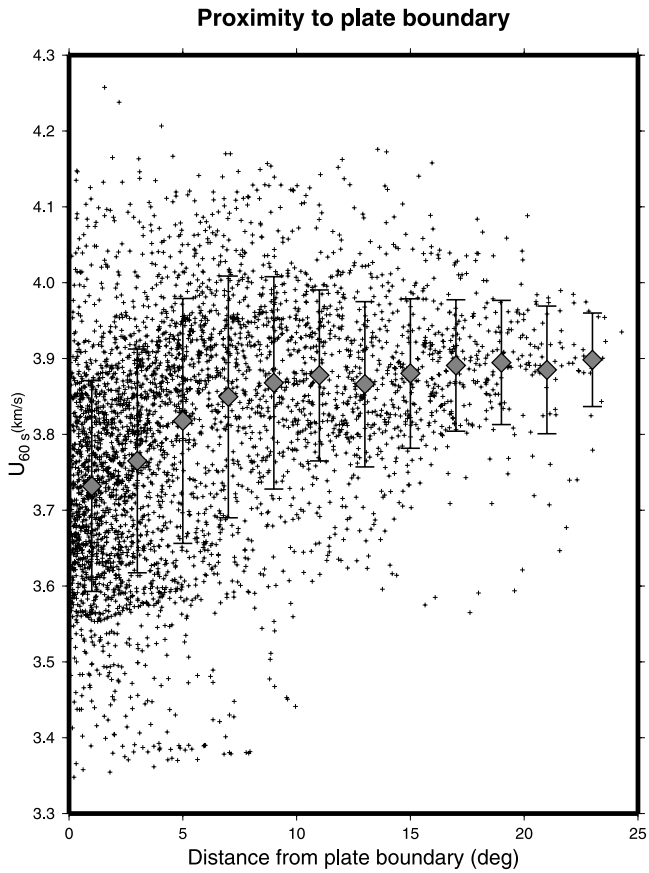

Figure 16. Correlation between 60 s Rayleigh wave group velocities (in km s^{-1}) and distance to nearest plate boundary (in degrees). Diamonds and bars indicate the mean and standard deviation of group velocity values in that distance range.

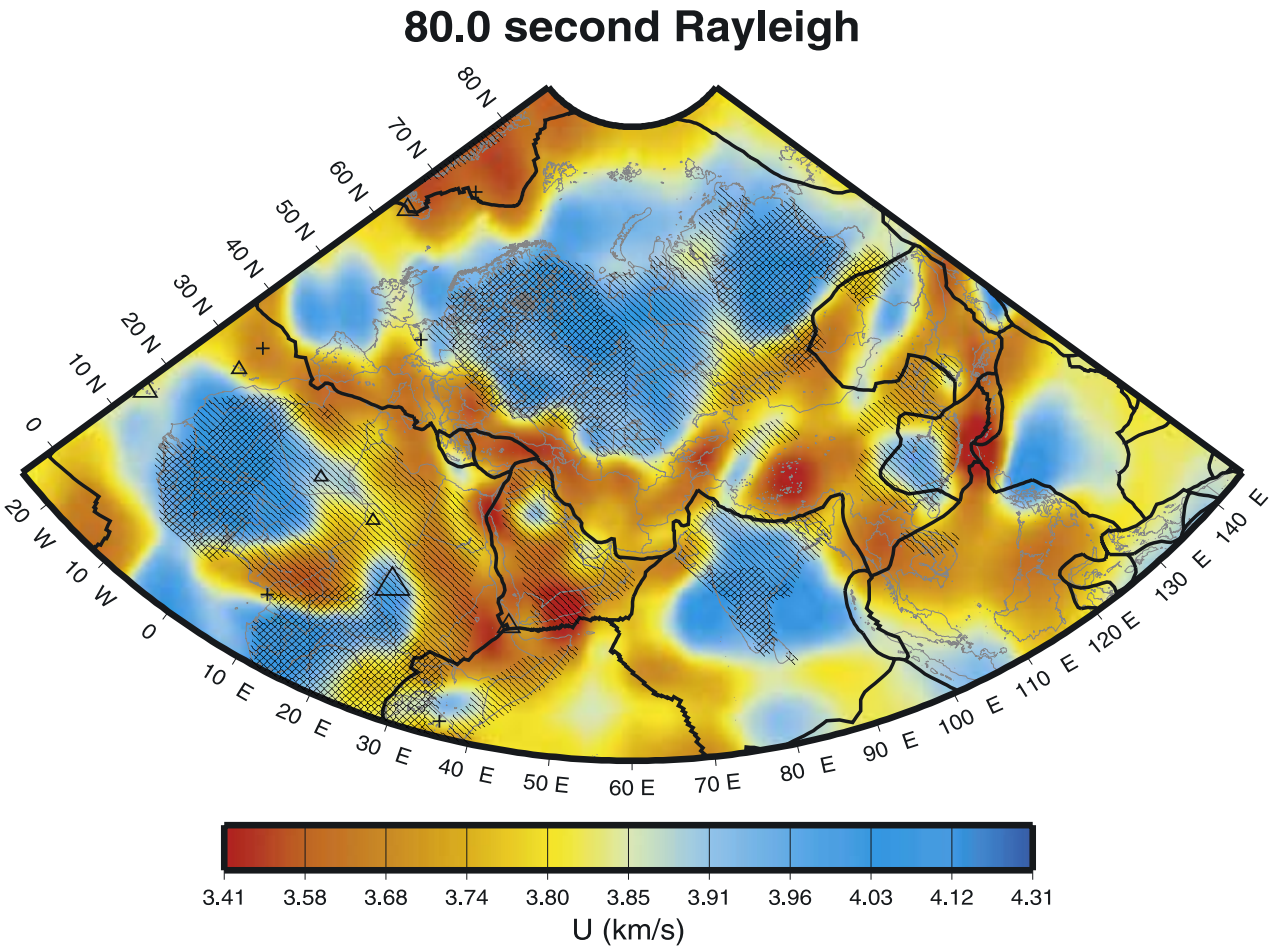

Figure 17. Map of 80 s Rayleigh wave group velocities shown with plate boundaries (thick lines), hot spots (triangles and crosses), and boundaries of platforms and cratons (hatched lines).

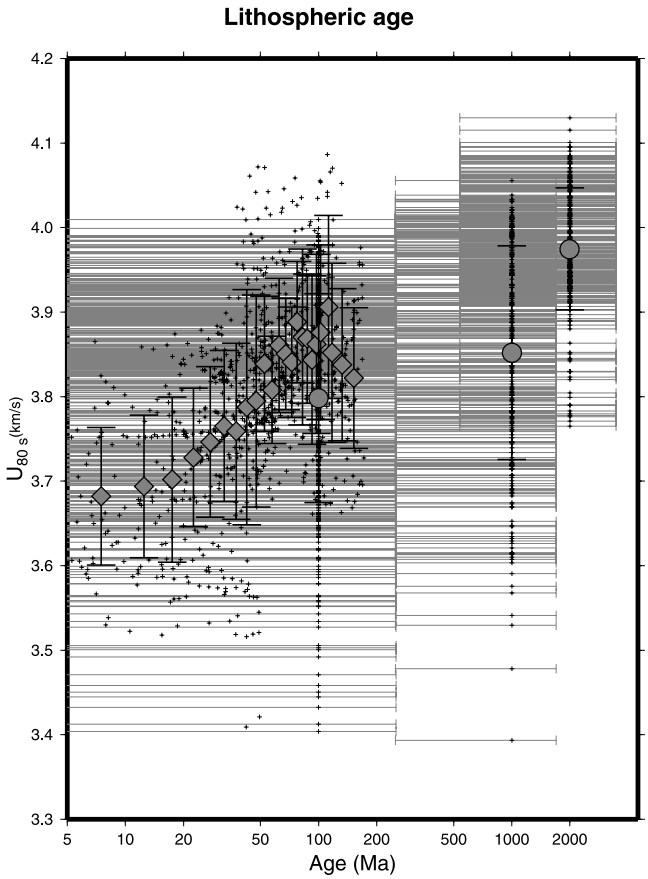

Figure 18. Correlation between 80 s Rayleigh wave group velocities (in km s^{-1}) and crustal age (in Ma). Gray bars indicate range of crustal age. The x axis is shown in logarithmic scale. Diamonds (for oceanic), circles (for continental) and their corresponding bars indicate the mean and standard deviation of group velocity values in that age range.

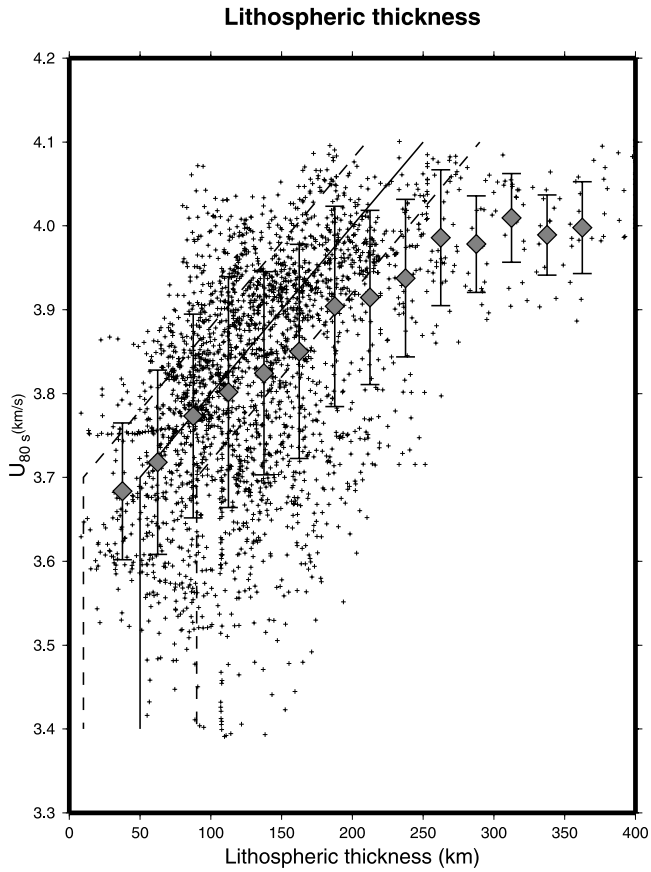

Figure 19. Correlation between 80 s Rayleigh wave group velocities (in km s^{-1}) and lithospheric thickness (in km). Diamonds and bars indicate the mean and standard deviation of group velocity values in that thickness range. The empirically derived relationship is shown in solid lines (mean) and dashed lines (mean ± standard deviation).

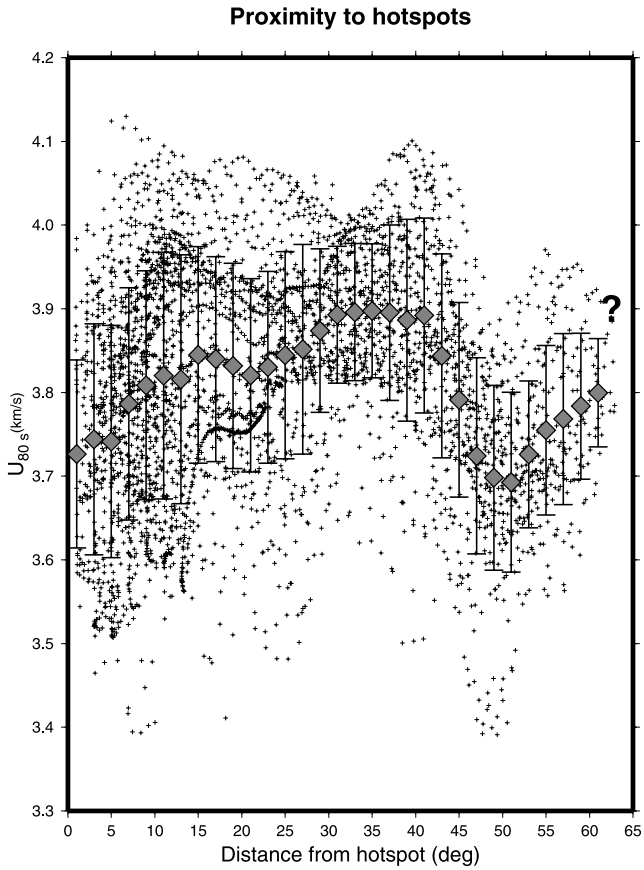

Figure 20. Correlation between 80 s Rayleigh wave group velocities (in km s^{-1}) and distance to nearest hot spot (in degrees). Diamonds and bars indicate the mean and standard deviation of group velocity values in that distance range.

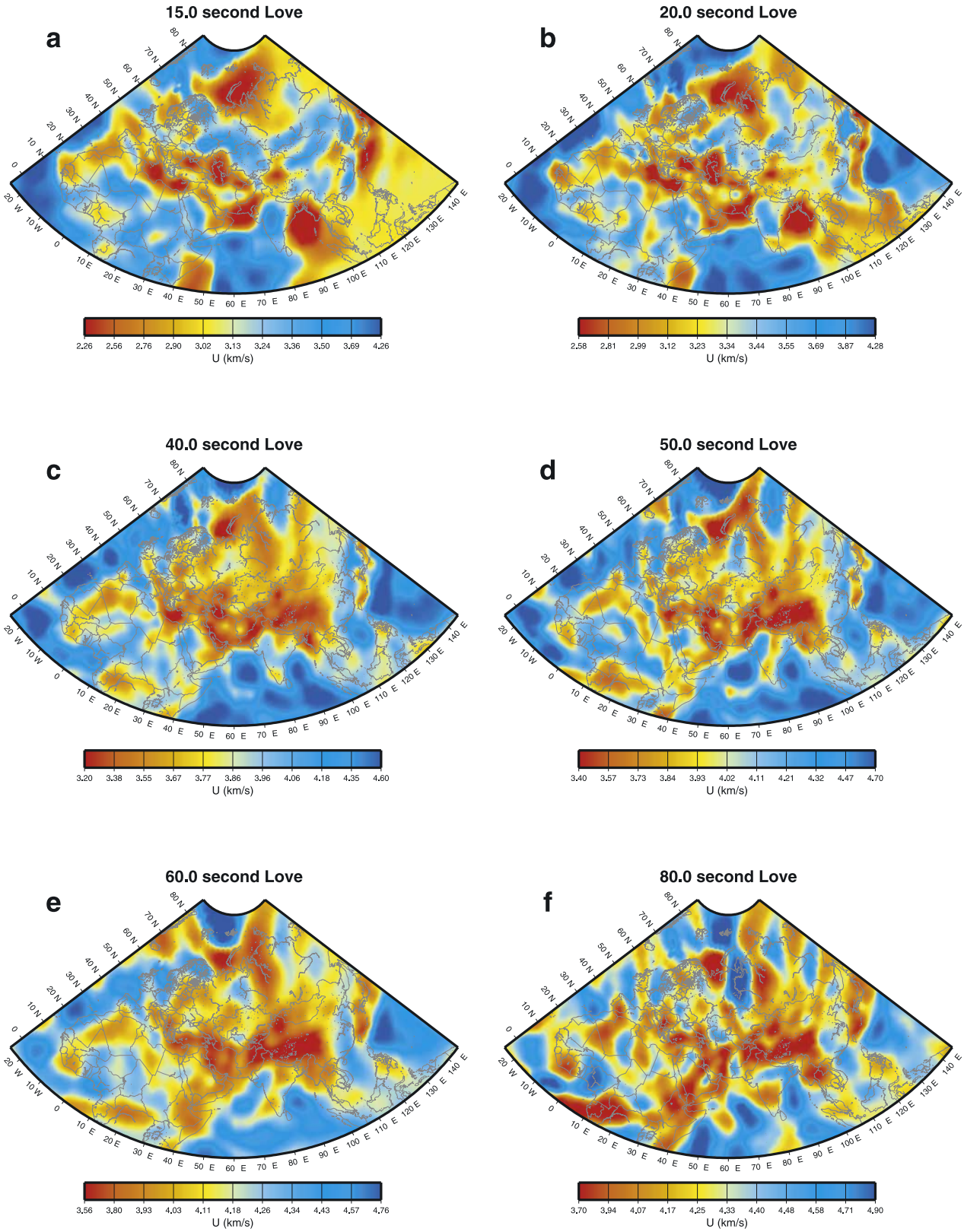

Figure 21. Inversion results for Love waves at (a) 15, (b) 20, (c) 40, (d) 50, (e) 60, and (f) 80 s.

Caucasus, Hindu Kush, and Himalayas. At periods longer than about 70 s (Figure 21f), the inversion results look spotty and do not correspond well to tectonic structure. There is also poorer continuity between adjacent periods than at shorter periods. This is due to the limited number of paths at these periods, as well as the higher uncertainties of the individual dispersion measurements. Inversion results at these periods have correspondingly higher uncertainties

associated with them, and will likely be improved only by increasing path coverage at these periods.

5. Conclusions

[30] We have measured surface wave group velocities for tens of thousands of paths in Eurasia, North Africa, and vicinity, and have combined this data set with measurements provided by other groups. By tomographically inverting the measurements, we find that Rayleigh and Love wave group velocity models, for periods ranging from 7 to 100 s, have significant lateral variations across the region. The results of this study are significantly higher resolution than any previous studies of the region performed on this scale. Using a variable smoothing presented here has allowed us to go to higher resolution where the data permit without introducing streaking or other artifacts of poor data coverage. This will become increasingly important as we continue to refine our model in some areas in response to improved data coverage.

[31] Even with the necessary coverage (both density and azimuth sampling), resolution is necessarily limited by the wavelength of the surface waves. From a purely geometrical argument, we could only hope to see resolutions finer than 2° for periods less than about 60 s and resolutions finer than 1° for periods <30 s. Of course, at very short periods we have poorer path coverage. The resolution of the models is probably greatest for 20–30 s Rayleigh waves, where we have a combination of excellent coverage and short wavelength. Even at these periods, we would only find the highest resolution in regions of dense coverage. Indeed, the maps appear best at these periods, where we are most likely to find small-scale features that correspond to tectonic features.

[32] Group velocity maps derived from our inversion correspond very well to tectonic structure throughout our expanded coverage area. As expected, short periods are sensitive to sediment thickness and intermediate periods exceptionally well correlated with crustal thickness. Long-period surface waves, being sensitive to upper mantle velocity, correspond closely to the age and temperature of lithospheric upper mantle. There is not a similar strong correlation to hot spots, although there could be a number of explanations for this.

[33] **Acknowledgments.** I would like to thank Bill Walter for his contributions to this work as well as giving the paper a critical reading, Mike Ritzwoller and Anatoli Levshin for providing their group velocity measurements, Chuck Ammon for providing the PGSWMFA code to make group velocity measurements, and Shannon Hazler and Maggie Benoit for making some of the dispersion measurements used in this study. I would also like to thank the Associate Editor, reviewer Jean-Jacques Leveque, and one anonymous reviewer for their helpful remarks. Figures were generated using the Generic Mapping Tools (GMT) software [*Wessel and Smith*, 1998]. Group velocity tomography results are available by contacting the author. This work was performed under the auspices of the U.S. Department of Energy by the University of California, Lawrence Livermore National Laboratory under contract W-7405-ENG-48. This is LLNL contribution UCRL-JRNL-210740.

References

Anderson, D. (1996), The edges of the mantle, in *The Core-Mantle Boundary Region*, *Geodyn. Ser.*, vol. 28, edited by M. Gurnis et al., pp. 255–271, AGU, Washington, D. C.

Artemieva, I. M., and W. D. Mooney (2001), Thermal structure and evolution of Precambrian lithosphere, *J. Geophys. Res.*, *106*, 16,387–16,414.

Bassin, C., G. Laske, and G. Masters (2000), The current limits of resolution for surface wave tomography in North America, *Eos Trans. AGU*, *81*(48), Fall Meet. Suppl., Abstract S12A-03.

Clift, P., and C. Gaedicke (2002), Accelerated mass flux to the Arabian Sea during the middle to late Miocene, *Geology*, *30*, 207–210.

Coffin, M. F., L. M. Gahagan, and L. A. Lawver (1998), Present-day plate boundary digital data compilation, *Tech. Rep. 174*, 5 pp., Univ. of Tex. Inst. for Geophys., Austin.

Debayle, E., and B. L. N. Kennett (2000), The Australian continent upper mantle: Structure and deformation inferred from surface waves, *J. Geophys. Res.*, *105*, 25,423–25,450.

Dziewonski, A. M., J. Bloch, and M. Landisman (1969), A new technique for the analysis of transient seismic signals, *Bull. Seismol. Soc. Am.*, *59*, 427–444.

Griffin, W. L., Z. Zhang, S. Y. O'Reilly, and C. G. Ryan (1998), Phanerozoic evolution of the lithosphere beneath the Sino-Korean Craton, in *Mantle Dynamics and Plate Interactions in East Asia*, *Geodyn. Ser.*, vol. 27, edited by M. Flower et al., pp. 107–126, AGU, Washington, D. C.

Herquel, G., G. Wittlinger, and J. Guilbert (1995), Anisotropy and crustal thickness of Northern-Tibet. New constraints for tectonic modeling, *Geophys. Res. Lett.*, *22*, 1925–1928.

Herrmann, R. B. (1973), Some aspects of band-pass filtering of surface waves, *Bull. Seismol. Soc. Am.*, *63*, 663–671.

Houseman, G. A., and P. Molnar (2001), Mechanisms of lithospheric rejuvenation associated with continental orogeny, in *Continental Reactivation and Reworking*, edited by J. A. Miller et al., *Geol. Soc. Spec. Publ.*, *184*, 13–38.

Huang, Z., W. Su, Y. Peng, Y. Zheng, and H. Li (2003), Rayleigh wave tomography of China and adjacent regions, *J. Geophys. Res.*, *108*(B2), 2073, doi:10.1029/2001JB001696.

King, S. D., and D. L. Anderson (1995), An alternative mechanism of flood basalt volcanism, *Earth Planet. Sci. Lett.*, *136*, 269–279.

Laske, G., and G. Masters (1997), A global digital map of sediment thickness, *Eos Trans. AGU*, *78*(46), Fall Meet. Suppl., F483.

Lees, J. M., and R. S. Crosson (1989), Tomographic inversion for three-dimensional velocity structure at Mount St. Helens using earthquake data, *J. Geophys. Res.*, *94*, 5716–5728.

Levshin, A. L., V. F. Pisarenko, and G. A. Pogrebinsky (1972), On a frequency-time analysis of oscillations, *Ann. Geophys.*, *28*, 211–218.

Levshin, A., J. Stevens, M. Ritzwoller, and D. Adams (2002), Short-period (7s–15s) group velocity measurements and maps in central Asia, paper presented at 24th Seismic Research Review: Nuclear Explosion Monitoring: Innovation and Integration, Natl. Nucl. Security Admin., Point Vedra Beach, Fla., 17–19 Sept.

Montelli, R., G. Nolet, F. A. Dahlen, G. Masters, E. R. Engdahl, and S.-H. Hung (2004), Finite-frequency tomography reveals a variety of plumes in the mantle, *Science*, *303*, 338–343.

Mooney, W. D., G. Laske, and T. G. Masters (1998), CRUST 5.1: A global crustal model at 5° × 5°, *J. Geophys. Res.*, *103*, 727–747.

Muller, R. D., W. R. Roest, J. Y. Royer, L. M. Gahagan, and J. G. Sclater (1997), Digital isochrons of the world's ocean floor, *J. Geophys. Res.*, *102*, 3211–3214.

Nataf, H.-C., and Y. Ricard (1996), 3SMAC: An a priori tomographic model of the upper mantle based on geophysical modeling, *Phys. Earth Planet. Inter.*, *95*, 101–122.

National Geophysical Data Center (1998), ETOPO-5 bathymetry/topography data, *Data Announcement 88–MGG-02*, NOAA, U.S. Dep. of Commer., Silver Spring, Md.

Parsons, B., and J. G. Sclater (1997), An analysis of the variation of ocean floor bathymetry and heat flow with age, *J. Geophys. Res.*, *82*, 803–827.

Pasyanos, M. E., W. R. Walter, and S. E. Hazler (2001), A surface wave dispersion study of the Middle East and North Africa for monitoring the Comprehensive Nuclear-Test-Ban Treaty, *Pure Appl. Geophys.*, *158*, 1445–1474.

Ritsema, J., and R. M. Allen (2003), The elusive mantle plume, *Earth Planet. Sci. Lett.*, *207*, 1–12.

Ritzwoller, M. H., and A. L. Levshin (1998), Eurasian surface wave tomography: Group velocities, *J. Geophys. Res*, *103*, 4839–4878.

Ritzwoller, M. H., N. M. Shapiro, A. L. Levshin, and G. M. Leahy (2001), Crustal and upper mantle structure beneath Antarctica and surrounding oceans, *J. Geophys. Res.*, *106*, 30,645–30,670.

Ritzwoller, M. H., N. M. Shapiro, M. P. Barmin, and A. L. Levshin (2002), Global surface wave diffraction tomography, *J. Geophys. Res.*, *107*(B12), 2335, doi:10.1029/2002JB001777.

Ritzwoller, M. H., N. M. Shapiro, and S.-J. Zhong (2004), Cooling history of the Pacific lithosphere, *Earth. Planet. Sci. Lett.*, *226*, 69–84.

Rudnick, R. L., and D. M. Fountain (1995), Nature and composition of the continental crust: A lower crustal perspective, *Rev. Geophys.*, *33*, 267–309.

Sclater, J. G., C. Jaupart, and D. Galson (1980), The heat flow through oceanic and continental crust and the heat loss of the Earth, *Rev. Geophys.*, *18*, 269–311.

Sleep, N. H. (1990), Hotspots and mantle plumes: Some phenomenology, *J. Geophys. Res.*, *95*, 6715–6736.

Spetzler, J., J. Trampert, and R. Snieder (2001), Are we exceeding the limits of the great circle approximation in global surface wave tomography?, *Geophys. Res. Lett.*, *28*, 2341–2344.

Spetzler, J., J. Trampert, and R. Snieder (2002), The effect of scattering in surface wave tomography, *Geophys. J. Int.*, *149*, 755–767.

Stein, C. A., and S. Stein (1992), A model for the global variation in oceanic depth and heat flow with lithospheric age, *Nature*, *359*, 123–129.

Turcotte, D. L., and G. Schubert (1982), *Geodynamics: Applications of Continuum Physics to Geological Problems*, 450 pp., John Wiley, New York.

Vdovin, O., J. A. Rial, A. L. Levshin, and M. H. Ritzwoller (1999), Group-velocity tomography of South America and the surrounding oceans, *Geophys. J. Int.*, *136*, 324–340.

Walter, W. R., and M. Ritzwoller (1998), Summary report of the workshop on the U.S. use of surface waves for monitoring the CTBT, *UCRL-ID-131835*, 16 pp., Lawrence Livermore Natl. Lab., Livermore, Calif.

Wessel, P., and W. H. F. Smith (1998), New, improved version of Generic Mapping Tools released, *Eos Trans. AGU*, *79*, 579.

Wiens, D. A., and G. P. Smith (2003), Seismological constraints on structure and flow patterns within the mantle wedge, in *Inside the Subduction Factory*, *Geophys. Monogr. Ser.*, vol. 138, edited by J. Eiler, pp. 59–82, AGU, Washington, D. C.

Yanovskaya, T. B., and V. M. Kozhevnikov (2003), 3D S-wave velocity pattern in the upper mantle beneath the continent of Asia from Rayleigh wave data, *Phys. Earth Planet. Inter.*, *138*, 263–278.

Yoshizawa, K., and B. L. N. Kennett (2002), Determination of the influence zone for surface wave paths, *Geophys. J. Int.*, *149*, 441–454.

Yuan, X., J. Ni, R. Kind, J. Mechie, and E. Sandvol (1997), Lithospheric and upper mantle structure of southern Tibet from a seismological passive source experiment, *J. Geophys. Res.*, *102*, 27,491–27,500.

Zhou, Y., F. A. Dahlen, and G. Nolet (2004), Three-dimensional sensitivity kernels for surface wave observables, *Geophys. J. Int.*, *158*, 142–168.

M. E. Pasyanos, Earth Science Division, Lawrence Livermore National Laboratory, P.O. Box 808, L-205, Livermore, CA 94551, USA. (pasyanos1@llnl.gov)